VIETNAM NATIONAL UNIVERSITY HO CHI MINH CITY
HO CHI MINH CITY UNIVERSITY OF TECHNOLOGY
FACULTY OF APPLIED SCIENCE
DEPARTMENT OF BIOMEDICAL ENGINEERING PHYSICS

CAPSTONE PROJECT

INVESTIGATION AND SIMULATION OF THE MECHANICAL BEHAVIOR OF HUMAN SKIN LAYERS WITH THE HYPERELASTIC MODEL USING THE FINITE ELEMENT METHOD

DINH HOANG DUY KHANH

Ho Chi Minh City, May 2025

VIETNAM NATIONAL UNIVERSITY HO CHI MINH CITY
HO CHI MINH CITY UNIVERSITY OF TECHNOLOGY
FACULTY OF APPLIED SCIENCE
DEPARTMENT OF BIOMEDICAL ENGINEERING PHYSICS

CAPSTONE PROJECT

INVESTIGATION AND SIMULATION OF THE MECHANICAL BEHAVIOR OF HUMAN SKIN LAYERS WITH THE HYPERELASTIC MODEL USING THE FINITE ELEMENT METHOD

Major: Engineering Physics – Specility: Biomedical Engineering

Student : Dinh Hoang Duy Khanh
ID number : 2153439
Instructors : Assoc. Prof. Dr. Tran Trung Nghia
Assoc. Prof. Dr. Nguyen Thanh Nha

Ho Chi Minh City, May 2025

VIETNAM NATIONAL UNIVERSITY HO CHI MINH CITY
HO CHI MINH CITY UNIVERSITY OF TECHNOLOGY
FACULTY OF APPLIED SCIENCE
DEPARTMENT OF
BIOMEDICAL ENGINEERING PHYSICS

SOCIALIST REPUBLIC OF VIETNAM
Independence – Freedom – Happiness

Ho Chi Minh City, May 05th, 2025

CAPSTONE PROJECT ASSIGNMENT

Student:	DINH HOANG DUY KHANH	**ID:**	2153439	**Class:**	CC21KYS2
Major:	Engineering Physics	**Specility:**	Biomedical Engineering		

1. Title of thesis:

Investigation and Simulation of The Mechanical Behavior of Human Skin Layers with The Hyperelastic Model using The Finite Element Method

2. Mission:

- Research and simulate Ogden hyperelastic materials using experimental data to select the most suitable parameters for the properties of human skin.
- Simulate the impact of microwave radiation through microwave cavity to the human skin layers model to investigate the absorption of the model
- Evaluation and assessment of replacing human skin with hyperelastic materials for certain practical biomedical applications.

3. Thesis assignment date: January 06th, 2025

4. Thesis completion date: May 05th, 2025

5. Instructors: - Assoc. Prof. Dr. Tran Trung Nghia
- Assoc. Prof. Dr. Nguyen Thanh Nha

The title and content of the graduation thesis have been approved by the Department of Biomedical Engineering Physics, Faculty of Applied Science.

INSTRUCTOR 1	**INSTRUCTOR 2**	**HEAD OF DEPARTMENT**
(Sign and write full name)	*(Sign and write full name)*	*(Sign and write full name)*

DECLARATIONS

Thesis title: Investigation and Simulation of The Mechanical Behavior of Human Skin Layers with The Hyperelastic Model using The Finite Element Method.

I, Dinh Hoang Duy Khanh (ID: 2153439), certify that this thesis is my own work, based on my personal study and/or research and that I have acknowledged all material and sources used in its preparation, whether they be books, articles, reports, lecture notes, and any other kind of document, electronic or personal communication.

I also certify that this thesis only submitted based on my scientific research for assessment in any academic capacity, and that I have not copied in part or whole or otherwise plagiarised the work of other persons.

I confirm that I have identified and declared all possible conflicts that I may have.

Signed and submitted

Student: Dinh Hoang Duy Khanh

ID number: 2153439

Date: May, 2025

ACKNOWLEDGEMENT

This thesis could not have been completed without the dedicated guidance of my supervisors, Assoc. Prof. Dr. Tran Trung Nghia and Assoc. Prof. Dr. Nguyen Thanh Nha. From the bottom of my heart, I sincerely thank you for your unwavering support, patience, and enthusiasm throughout the duration of this thesis.

In addition, I would like to express my gratitude to the lecturers of the Department of Biomedical Engineering Physics and the Department of Engineering Mechanics in Ho Chi Minh City University of Technology (HCMUT) - VNU-HCM for their dedicated teaching and guidance during my undergraduate program. Furthermore, I appreciate the insightful feedback provided by Prof. Dr. Truong Tich Thien, Dr. Le Quoc Khai, Dr. Trinh Tran Hong Duyen, M.S. Le Nhat Tan, and M.S. Nguyen Ngoc Hai helped improve this thesis's quality.

I am grateful to my colleagues and fellow researchers for their constructive feedback and collaboration, which helped refine the ideas and methodologies presented in this thesis. Thanks to my best team from Major in Biomedical Engineering: Dao Minh Khanh Tuyen, Tran Tam Nha, Nguyen Trung Thach, Tran Huynh Gia Huy, Tran Huynh Thien Phu, Pham Viet Khiem; and my wonderful team from Major in Engineering Mechanics: Trinh Gia Khang, Vu Nguyen Hoang, Vo Thanh Luan, Nguyen Tran Thien An, Vu Hoang Kha Vy, Hoang Quoc Thai, Huynh Thach Thao, Le Thanh.

Nevertheless, I am so grateful to Laboratory of Numerical Simulation VIBE Project (503-B4) and Laboratory of General Physics (201-B6) for the academic environment and their contributions for this field.

Finally, I want to extend my heartfelt thanks to my family, friends, and loved ones for their encouragement, support, and genuine affection, which have been a source of motivation for me to complete this thesis.

ABSTRACT

In biomechanical study, the intricate nature of human skin presents substantial untapped potential due to its biological structure, particularly in simulation and computational biomechanics. Previous studies have produced approximate results using second-order Ogden material for the human body. However, there is still a lack of computational evidence to demonstrate that the Ogden model is consistently suitable to replace human or artificial skin. Moreover, the material's mechanical characteristics remain a challenging issue in accurately determining the material parameters used in simulation studies. This paper employs the Ogden formulation as a hyperelastic material model for simulating human skin. Utilizing reference data from prior studies, the nonlinear finite element method (FEM) is employed for analyzing large deformations of the skin model. A thin plate simulates a 3D skin model with a finer mesh and takes the boundary conditions. This study aims to juxtapose experimental data with in vivo mechanical properties by employing Ogden's coefficients to simulate the behavior of the skin model using the finite element method with an Analysis System (ANSYS). The obtained numerical model effectively illustrates the nonlinear behavior of the skin. Furthermore, the experiment also simulates how human skin absorbs energy—using material parameters that were determined in earlier studies—within a microwave-cavity environment. In general, all of the results from experiments can show the mechanical behavior of the hyperelastic model. The numerical results show the utility of these parameters in human skin simulation in 2D and 3D elements (SOLID186) and illustrate an approximate bow wave shape and the occurrence of wrinkling in the test area, which is considered an artificial human skin model. Building a microwave-cavity model will make it possible to evaluate how the chosen hyperelastic material absorbs energy, thereby facilitating the assessment and comparison of experimental data.

TÓM TẮT

Trong nghiên cứu cơ sinh học, cấu trúc phức tạp của da người thể hiện tiềm năng chưa được khai thác đáng kể do tính chất sinh học đặc thù, đặc biệt là trong các nghiên cứu mô phỏng và cơ sinh học tính toán. Các nghiên cứu trước đây đã thu được kết quả xấp xỉ khi sử dụng vật liệu Ogden bậc hai để mô hình hóa cơ thể người. Tuy nhiên, vẫn còn thiếu các bằng chứng tính toán cho thấy mô hình Ogden có thể nhất quán và phù hợp để thay thế cho da người hoặc da nhân tạo. Bên cạnh đó, các đặc tính cơ học của vật liệu này vẫn là một vấn đề khó khăn trong việc xác định chính xác các tham số vật liệu được sử dụng trong các nghiên cứu mô phỏng.

Luận văn này sử dụng công thức Ogden như một mô hình vật liệu siêu đàn hồi để mô phỏng da người. Dựa trên dữ liệu tham khảo từ các nghiên cứu trước, phương pháp phần tử hữu hạn phi tuyến (FEM) được áp dụng để phân tích biến dạng lớn của mô hình da. Một tấm mỏng được sử dụng để mô phỏng mô hình da 3D với lưới chia mịn và có tính đến các điều kiện biên. Mục tiêu của nghiên cứu là so sánh dữ liệu thực nghiệm với các đặc tính cơ học in vivo bằng cách sử dụng các hệ số Ogden để mô phỏng hành vi của mô hình da thông qua phương pháp phần tử hữu hạn trong phần mềm phân tích Ansys.

Mô hình số thu được thể hiện hiệu quả hành vi phi tuyến của da. Ngoài ra, thí nghiệm cũng mô phỏng cách da người hấp thụ năng lượng — sử dụng các tham số vật liệu đã được xác định từ các nghiên cứu trước — trong môi trường cộng hưởng vi ba. Nhìn chung, tất cả các kết quả từ thí nghiệm đều có thể phản ánh hành vi cơ học của mô hình vật liệu siêu đàn hồi. Kết quả mô phỏng cho thấy tính ứng dụng của các tham số này trong việc mô phỏng da người với các phần tử 2D và 3D (SOLID186), đồng thời tái hiện hình dạng sóng cung xấp xỉ cũng như hiện tượng nhăn tại vùng thử nghiệm — được xem như là mô hình da người nhân tạo. Việc xây dựng mô hình cộng hưởng vi ba sẽ cho phép đánh giá khả năng hấp thụ năng lượng của vật liệu siêu đàn hồi đã chọn, từ đó hỗ trợ việc phân tích và so sánh dữ liệu thực nghiệm.

TABLE OF CONTENTS

LIST OF FIGURES

LIST OF TABLES

LIST OF ABBREVIATIONS AND MATHEMATICS SYMBOLS

FEM	Finite Element Method
FEA	Finite Element Analysis
HFSS	High Frequency Simulation Software
SAR	Specific Absorption Rate
DC	Direct Current
AC	Alternating Current
RF	Radiation Frequency
W	Strain energy
$\lambda_1, \lambda_2, \lambda_3$	Principal stretch
$\alpha_1, \alpha_2, \alpha_3$	Ogden material exponent
μ_1, μ_2, μ_3	Ogden material parameter
S	Second Piola-Kirchhoff stress tensor
$E_{\alpha\beta}$	Deformation of a thin plate
E	Young's modulus
g	Post-deformation coefficient
G	Pre-deformation coefficient
σ	Cauchy stress tensor
φ	Rotation angle for isotropic materials
p	Pressure constant
n	Unit vector
$x_{,\alpha}, x_{,\beta}$	Normal vector
N	Isoparametric element of the shape function
n_c	Number of nodes per element
S^h	Stress vector
K	Tangent stiffness matrix
J	Jacobian matrix
t_i	Orthogonal system
ε	Permitivity of material
δ	Characteristic penetration depth

CHAPTER 1: INTRODUCTION

1.1 Problem statement

The skin is the largest organ of the human body, covering the entire surface and performing various essential physiological functions. It consists of three primary layers: epidermis, dermis, and hypodermis (subcutaneous tissue). Each layer serves distinct roles but works synergistically to protect the body, regulate temperature, and respond to external stimuli. Additionally, the skin exhibits anisotropy, meaning its mechanical properties vary depending on the direction of the applied force. It also demonstrates heterogeneity due to differences in thickness and composition across various regions of the body. These complex features make the modeling and analysis of skin more challenging compared to other biological tissues. An important aspect of skin research is its viscoelastic behavior, which causes the skin to exhibit different responses depending on the duration and speed of applied forces. Under short-term stress, the skin stretches and responds quickly, while prolonged loading leads to deformation that may not be fully reversible. This behavior arises from the interaction between collagen and elastin fibers within the dermis. Moreover, factors such as age, moisture levels, temperature, and environmental conditions influence these properties, adding further complexity. As a result, skin behaves as a nonlinear, unpredictable biological material.

The study of the mechanical properties of human skin has significant implications beyond medicine and biology, finding applications across diverse industries. For example, in the cosmetics industry, understanding the structure of the skin enables manufacturers to develop more effective skincare products by optimizing the penetration of active ingredients. In animation and simulation technologies, the elasticity and deformability of human skin are critical in creating realistic character movements. Furthermore, in the design of skin-contact devices, such as razors, seats, and surgical instruments, knowledge of the skin's mechanical behavior helps enhance user comfort and prevent damage caused by friction or abrasion.

Despite numerous studies aiming to understand the properties of human skin, the current knowledge remains limited in constructing accurate models for specific applications. The mechanical models often struggle to fully capture the skin’s complex characteristics, such as heterogeneity, anisotropy, and time-dependent behavior. Additionally, the variations in skin thickness and properties across different body regions further complicate the development of generalized models. Therefore, there is a pressing need for advanced tools and

methodologies to collect more precise data. A deeper understanding of the factors influencing skin mechanics will not only improve product design but also open new avenues for interdisciplinary research in the future.

Therefore, experimental research to determine the properties of the skin remains the key to gaining a deeper understanding of its behavior. However, conducting such experiments is time-consuming, costly, and no current experiment can be considered a standard, despite recent studies showing some progress in providing better insights into the unique characteristics of the skin. On the other hand, the applications are intended to serve humans, but conducting experiments directly on living human skin is extremely difficult and complex.

With the development of computational methods, computer science, and the advent of structural analysis software based on the finite element method (e.g., ANSYS, ABAQUS, COMSOL, SYSTY, etc.), human skin models can be constructed, and their mechanical properties and material parameters can be identified. This enables the creation of standardized models, forming the basis for future experiments.

1.2 Objectives

As mentioned in the previous section, the objective of this thesis is to determine the material constants and develop a finite element model (FEM) for simulating human skin. Building a finite element model helps reduce the cost and time associated with conducting experiments on real models, which are inherently complex. In this study, the human skin model is assumed to be a nonlinear material with the characteristics of hyperelastic material and subjected to large deformations.

Once the material constants are obtained through finite element simulations, the researcher will conduct several applied simulations to describe the behavior of human skin in the microwave radiation with simulations of microwave cavity with the numerical model.

1.3 Research subjects and scopes

Subject: The thin plate based on the Ogden hyperelastic model and the microwave cavity with three layers of model.

Scope: ANSYS High Frequency Simulation Software and ANSYS Workbench (Stastic Structures).

1.4 Significance

This study of human skin mechanics, particularly through the development of finite element models (FEM), holds considerable importance for both scientific research and practical applications. Accurately modeling human skin as a nonlinear, hyperelastic material subjected to large deformations offers several benefits. Firstly, it enables a deeper understanding of the skin's mechanical behavior without the need for expensive and time-consuming physical experiments. This is particularly crucial, as conducting experiments directly on living tissue is both complex and ethically challenging.

The ability to determine material constants through FEM simulations provides essential data for various real-world applications, such as optimizing the treatment of open wounds using skin-stretching devices. Such simulations can aid medical practitioners in designing more effective interventions, improving patient outcomes, and minimizing healing times. Furthermore, this research contributes to the development of medical devices, prosthetics, and other technologies that interact with human skin, ensuring better comfort, durability, and performance.

The outcomes of this study are not only significant in medical and healthcare fields but also extend to industries such as cosmetics, biomechanics, and animation, where understanding skin behavior under deformation can enhance product design and innovation. Ultimately, this research lays the foundation for future advancements in skin-related technologies, offering both scientific insight and practical value across multiple disciplines.

1.5 Research status

The simulation of the mechanical behavior of human skin using hyperelastic models and the finite element method (FEM) has been a growing area of interest in recent decades. Researchers have sought to capture the complex, nonlinear characteristics of skin—particularly its viscoelastic and anisotropic properties [1]—to better understand its responses under various mechanical loads [2]. This has implications for applications ranging from medical device design to cosmetic and surgical interventions.

Early studies primarily used linear elastic models to approximate skin behavior, which oversimplified the skin's response to stress and strain. Over time, researchers moved toward hyperelastic models, such as the Ogden [3], Mooney-Rivlin [4], and Neo-Hookean [5] models, which better represent the skin's non-linear elastic behavior, especially under large deformations. Recent advancements have refined these models by calibrating material

constants specific to skin's unique structural makeup. Notably, the Ogden model has been widely adopted due to its flexibility in adjusting parameters to fit experimental data on skin's mechanical response.

FEM has become the preferred approach for simulating skin due to its versatility in modeling complex geometries and materials [6]. FEM allows researchers to layer different material properties corresponding to the epidermis, dermis, and hypodermis, accurately representing the heterogeneity of skin. Studies have shown that multi-layered FEM models, combined with hyperelastic material assumptions, yield simulations that closely match experimental data on skin's deformation under pressure, tension, and shear forces. There has been significant progress in applying FEM-based skin simulations in medical fields, particularly for surgical planning, wound healing, and prosthetic design. Simulations of skin deformation under various loading conditions assist in optimizing device shapes and materials, ensuring better biocompatibility and reducing skin irritation. Additionally, the cosmetics industry leverages microwave cavity models in human skin to predict how electromagnetic energy interacts with various skin layers [7], enhancing product safety and efficacy. Researchers have also explored the skin's response to microwave exposure in human skin, demonstrating that FEM simulations within a microwave cavity framework can serve as powerful tools for predicting and visualizing localized tissue heating, structural damage, or healing processes.

1.6 Expected outcomes and thesis structure

Based on the objectives of the study, this thesis aims to develop a finite element model (FEM) for human skin and determine the material parameters of human skin using the Ogden material model. These models and material parameters will then be utilized in future experiments, particularly in the fields of biomedical engineering and biomechanics.

The structure of the thesis is divided into five chapters, as follows:

- *Chapter 1* provides a brief introduction to the structure of human skin, the research objectives, research methods, the scope and subjects of the study, expected outcomes, and the thesis structure.
- *Chapter 2* presents the Ogden material model, the equations, and methods for constructing the Ogden material model for thin membrane sheets.
- *Chapter 3* describes in more detail the method for determining human skin displacement through experimental data. It also introduces the two finite element

types, PLANE183 and SOLID186, the microwave cavity with wave port, and elaborates on the research subjects of the thesis.

- *Chapter 4* offers a detailed simulation to validate the material parameters using the finite element method. It outlines the process and results of FEM simulations for human skin. Also provides remarks and conclusions regarding the achievements, limitations, and future directions of the thesis.
- *Chapter 5* presents the microwave caivity simulation and the absorption in each human skin layers based on the previous model.
- *Chapter 6* provides remarks and conclusions regarding the achievements, limitations, and future directions of the thesis.

CHAPTER 2: THEORETICAL BASIS

2.1 Hyperelastic material for human skin model

2.1.1 Hyperelastic material

A hyperelastic material is defined by its elastic strain energy density W_s, which is a function of the elastic strain state. It is often referred to as energy density. The hyperelastic formulation normally gives a nonlinear relation between stress and strain, as opposed to Hooke's law in linear elasticity. Most of the time, the right Cauchy–Green deformation tensor C is used to describe the current state of strain (although one could use the left Cauchy–Green tensor B, the deformation gradient tensor F, and so forth), so the strain energy density is written as $W_s(C)$.

For isotropic hyperelastic materials, any state of strain can be described in terms of three independent variables — common choices are the invariants of the right Cauchy–Green tensor C, the invariants of the Green–Lagrange strain tensor, or the principal stretches. Once the strain energy density is defined, the second Piola–Kirchhoff stress is computed as:

$$S = 2\frac{\partial W_s}{\partial C} \tag{2.1}$$

2.1.2 Choosing the hyperelastic material for human skin model

The study of elasticity began with classical linear elasticity, which was first formalized by Robert Hooke in 1678 with Hooke's Law [8]. This law describes the linear relationship between stress and strain in elastic materials under small deformations. However, as researchers investigated materials like rubber and biological tissues, it became evident that linear elasticity could not adequately model the large, nonlinear deformations these materials experienced. The transition from linear to nonlinear elasticity was significantly influenced by the works of Augustin-Louis Cauchy and Siméon Denis Poisson [9] in the early 19th century. They expanded the elasticity framework by introducing concepts of strain energy density functions, which laid the foundation for future developments in nonlinear material modeling.

The concept of hyperelasticity emerged in the mid-20th century, driven by the need to model large deformations in rubber-like materials. Ronald Rivlin made significant contributions to this field in the 1940s and 1950s. Rivlin proposed a strain energy density function for isotropic incompressible materials, leading to the development of the Neo-

Hookean and Mooney-Rivlin models. These models became some of the earliest hyperelastic material models and are still widely used today for rubber and soft tissues.

In the 1970s, Ray W. Ogden introduced a more versatile hyperelastic model known as the Ogden model [10]. This model expanded the range of materials that could be accurately represented, including highly nonlinear materials like biological tissues and polymers. The Ogden model uses multiple pairs of material constants (μ and α) to describe the strain energy density, allowing it to capture complex stress-strain behaviors under large deformations. The Ogden model has been particularly influential in biomechanics, where it has been used extensively to model soft tissues such as skin, muscles, and arteries.

2.1.3 Introduction to Ogden material

2.1.3.1 Briefly about Raymond William Ogden

Raymond William Ogden, born on September 19th, 1943, is a distinguished British applied mathematician renowned for his contributions to the nonlinear theory of elasticity. He holds the title of Emeritus George Sinclair Professor of Mathematics at the University of Glasgow. Ogden's research has significantly advanced the understanding of nonlinear elasticity, particularly in modeling the mechanical behavior of rubber-like materials and biological tissues. He is best known for developing the Ogden material model, which describes the complex stress-strain relationships in hyperelastic materials. This model has been widely adopted in both academic research and industrial applications.

Figure 2.1 Professor Raymond W. Ogden in 2006

Ogden's dissertation focused on the topic "Constitutive Relations for Elastic and Plastic Materials". After completing his doctoral program in 1970, he became a research fellow at the University of East Anglia, UK. In 1972, he published a scientific paper titled "Large Deformation Isotropic Elasticity: On the Correlation of Theory and Experiment for Compressible Rubber-like Solids" [10].

Ogden argued that representing strain energy as a function of multiple independent strain variables unnecessarily complicates mathematical analysis, particularly when calculating the instantaneous elastic modulus. Instead, he directly utilized the principal stretches as independent variables to formulate the strain energy equation. This approach led to a model that was sufficiently simple for mathematical analysis while also accurately representing the mechanical properties of compressible rubber-like materials. Furthermore, the paper demonstrated a strong agreement between theoretical predictions and experimental data.

2.1.3.2 Ogden material model

In 1972, Ogden proposed what is now widely known as the “Ogden model” [10]. His goal was to develop a material model that would meet two key criteria: (i) it would provide accurate predictions for isotropic, incompressible, rubber-like materials subjected to large deformations, and (ii) it would offer a more mathematically tractable alternative to models based on strain invariants. Ogden assumed that rubber-like materials could be idealized as hyperelastic—materials that exhibit no hysteresis, where the stress depends solely on the current strain and not on the strain history. The strain-energy function he introduced is typically expressed as:

$$W(\lambda_1,\lambda_2,\lambda_3)=\sum_{i=1}^{n}\mu_i\frac{\lambda_1^{\alpha_i}+\lambda_2^{\alpha_i}+\lambda_3^{\alpha_i}-3}{\alpha_i},(1\le n<m) \tag{2.2}$$

where α_i and μ_i are material parameters, and the principal stretches are related as follows:

$$\lambda_1\lambda_2\lambda_3=1 \tag{2.3}$$

The strain energy function (2.2) for the Ogden material reduces to the strain energy function of the Mooney-Rivlin material when the material parameters satisfy the following conditions:

$$m=2,\alpha_1=2,\alpha_2=-2;\ \mu_1=2C_1,\ \mu_2=2C_2 \tag{2.4}$$

or:

$$m=2,\alpha_1=-2,\alpha_2=2;\ \mu_1=2C_1,\ \mu_2=2C_2 \tag{2.5}$$

where C_1 and C_2 are the material constants of the Mooney-Rivlin model.

By using principal stretches as independent variables, Ogden avoided relying on the traditional strain invariants I_1 and I_2, which he believed was unnecessarily complicated mathematical analysis [4]. The model is classified based on the value of n: it is referred to as the one-term Ogden model when $n=1$, the two-term Ogden model for $n=2$, and so on. Notably, with specific parameter selections, the Ogden model can replicate both the Neo-Hookean and Mooney-Rivlin models. As a result, the one-term Ogden model provides a significantly better fit to experimental data for natural rubber compared to the Neo-Hookean model, while also offering a simpler mathematical framework than other two-parameter models, without sacrificing accuracy. Due to its effectiveness in modeling rubber-like materials, its simplicity, and its strong alignment with experimental results, the Ogden model quickly gained widespread adoption, leading to this special issue commemorating its 50th anniversary.

2.1.3.3 Applications and limitations of Ogden model

The Ogden model is highly versatile and widely applicable across various types of hyperelastic constitutive relationships. It is particularly effective in providing accurate simulations over the entire range of strain deformation for rubber-like materials [11].

Ideal for large deformation problems: The Ogden model is well-suited for describing large deformation scenarios. In higher-order formulations, it achieves remarkable accuracy even when strains reach up to 700%. This makes it a preferred choice for applications where extreme deformations are expected.

Suitable for modeling discontinuous shear modulus and compressible material behavior: The model can effectively capture the behavior of materials with discontinuous shear moduli, as well as the mechanical response of compressible materials. This capability ensures its applicability to a wide range of engineering and biomechanical problems.

Captures rapid stiffness increase at high strain levels: One of the unique strengths of the Ogden model is its ability to describe the rapid increase in material stiffness observed in the later stages of deformation. This feature is crucial for accurately simulating the behavior of materials under extreme loading conditions, where traditional models might fail.

Limitations in predicting deformations across different loading modes: The material constants derived from a specific type of experimental test (e.g., uniaxial tension) may not reliably predict the material's behavior under different deformation modes (e.g., biaxial or shear loading). Therefore, the Ogden model is not recommended for use in cases where

insufficient experimental data is available, such as when only uniaxial tensile test data is provided.

2.2 Structure of skin layers in human body

Human skin is classified as a complex tissue, consisting of multiple distinct layers: the epidermis, the dermis—divided into the superficial papillary dermis and the collagen-dense reticular dermis—and the hypodermis, which comprises subcutaneous fat. The epidermis is identified as a key component of the skin's barrier function, responsible for minimizing evaporative fluid loss and shielding the body from harmful substance penetration [12].

The epidermis is composed of several distinct layers, arranged from the deepest to the most superficial: the stratum basale, stratum spinosum, stratum granulosum, stratum lucidum, and stratum corneum. The deepest layer, the stratum basale (or stratum germinativum), is separated from the dermis by the basement membrane, also known as the basal lamina, and is attached to the dermis via hemidesmosomes. This layer consists of cuboidal to columnar cells, which function as mitotically active stem cells responsible for the continuous production of keratinocytes, ensuring the regeneration of the epidermis. Additionally, melanocytes, which synthesize melanin—the pigment that determines skin color—are present in this layer.

Above the stratum basale lies the stratum spinosum, also known as the prickle cell layer. This layer comprises 8 to 10 layers of irregularly shaped polyhedral cells with cytoplasmic projections, or "spines," that form desmosomal connections with neighboring cells. These desmosomes provide mechanical strength and structural cohesion to the epidermis. The stratum spinosum also contains dendritic cells, which play a key role in the immune response by identifying and processing antigens.

The dermis, located beneath the epidermis and connected to it via the basement membrane, is composed of two distinct layers of connective tissue: the papillary layer and the reticular layer, which merge without a clear boundary. The papillary layer, the uppermost portion of the dermis, consists of loose connective tissue and is in direct contact with the epidermis. This layer is rich in capillaries, small blood vessels, and nerve endings, contributing to sensory perception and providing nutrients to the epidermis.

Beneath the papillary layer lies the reticular layer, which is thicker and composed of dense connective tissue characterized by large bundles of collagen fibers. These fibers provide tensile strength and elasticity to the skin. The reticular layer also contains essential

structures, including sweat glands, hair follicles, arrector pili muscles, sensory neurons, and blood vessels. These components play crucial roles in thermoregulation, sensory reception, and maintaining overall skin health.

The hypodermis, also referred to as the subcutaneous fascia, is situated beneath the dermis and represents the deepest layer of the skin. This layer primarily consists of adipose tissue, which is organized into lobules. These adipose lobules function as an energy reserve, provide insulation, and offer cushioning to protect underlying structures. In addition to adipose tissue, the hypodermis contains sensory neurons, which contribute to the detection of pressure and vibration, and blood vessels that help regulate body temperature and supply nutrients to the skin. Although the hypodermis houses fewer skin appendages than the dermis, it does contain some hair follicles and associated structures [13].

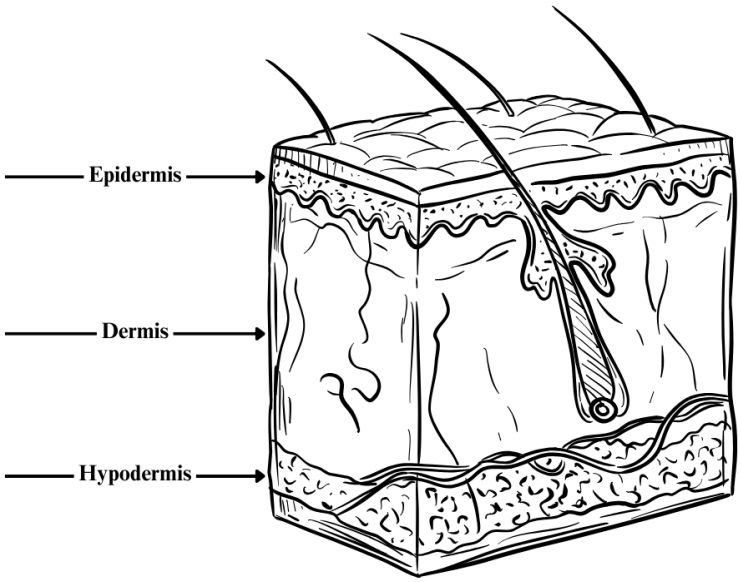

Figure 2.2 The diagram structure of human skin on the body contains 3 main layers: epidermis, dermis, and hypodermis

2.3 Ogden material model with thin plate

2.3.1 Stress calculation

This section presents the constitutive equations for materials with properties similar to incompressible rubber-like materials. The application of these equations to thin membranes and the linearization of stress-strain relationships are also discussed.

The coordinates of points on the surface of the thin membrane are denoted as (ξ,η) (local coordinate system). The current position vector is given by: $x(\xi,\eta) = x_i e_i$ while the initial position vector is: $X(\xi,\eta) = X_i e_i$. These two positions are related through the expression:

$x = X + u$, where $u = u_i e_i$ represents the displacement vector, with components associated with the Cartesian coordinate system e_i. The strain tensor $E_{\alpha\beta}$ for the thin plate is then determined using the following equation:

$$E_{\alpha\beta} = \frac{1}{2}\left(\frac{\partial u_\alpha}{\partial X_\beta} + \frac{\partial u_\beta}{\partial X_\alpha} + \frac{\partial u_\gamma}{\partial X_\alpha}\frac{\partial u_\gamma}{\partial X_\beta} \right) \tag{2.6}$$

or:

$$E_{\alpha\beta} = \frac{1}{2}\left(g_{\alpha\beta} - G_{\alpha\beta} \right) \tag{2.7}$$

where $g_{\alpha\beta}$ and $G_{\alpha\beta}$ are the coefficients after deformation and before deformation, respectively [4], and are defined by the following equation:

$$g_{\alpha\beta} = x_{,\alpha} \cdot x_{,\beta} \quad \text{and} \quad G_{\alpha\beta} = X_{,\alpha} \cdot X_{,\beta}$$

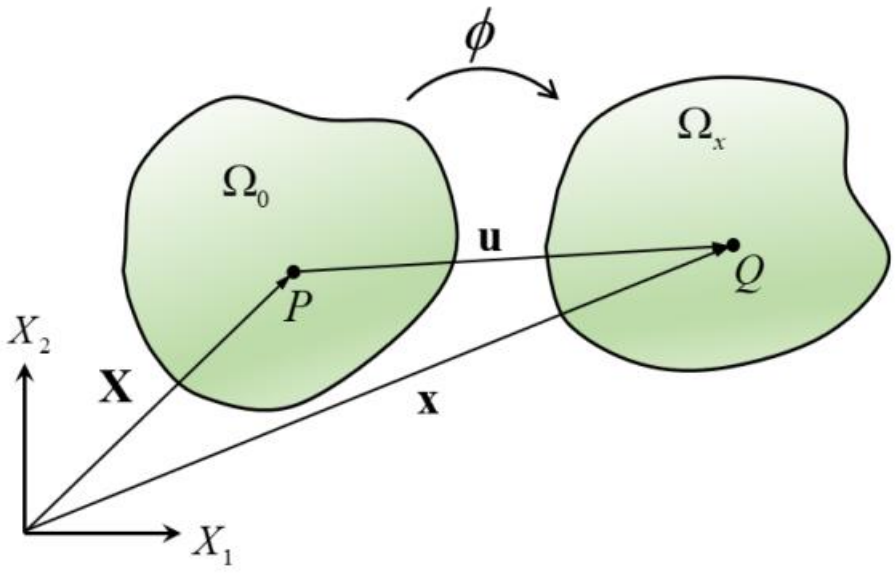

Figure 2.3 The continuous model before and after deformation

Using the equation (2.8) the principal stretches λ_1 and λ_2 can be determined. Since the stretch tensor U can be obtained through the symmetric Cauchy-Green tensor $\mathbf{C}$, where $\mathbf{C} = \mathbf{U}^2$, the principal stretches λ_α will be identified through an orthogonal transformation:

$$\mathbf{C} = \mathbf{R}\mathbf{C}\mathbf{R}^T \tag{2.8}$$

where:

$$\mathbf{C} = \begin{bmatrix} g_{11} & g_{12} \\ g_{21} & g_{22} \end{bmatrix}, \quad \mathbf{R} = \begin{bmatrix} \cos\varphi & -\sin\varphi \\ \sin\varphi & \cos\varphi \end{bmatrix}, \quad \mathbf{C} = \begin{bmatrix} \lambda_1^2 & 0 \\ 0 & \lambda_2^2 \end{bmatrix} \tag{2.9}$$

Using the incompressibility condition (2.3), equation (2.2) depends only on the principal stretches λ_1 and λ_2:

$$W(\lambda_r) = \sum_r \frac{\mu_r}{\alpha_r}\left[\lambda_1^{\alpha_r} + \lambda_2^{\alpha_r} + (\lambda_1\lambda_2)^{-\alpha_r} - 3\right] \tag{2.10}$$

When the model is assumed to be a hyperelastic material, the second Piola-Kirchhoff stress tensor $\mathbf{S}$ is the derivative of the strain energy density function W with respect to the strain components:

$$S^{\alpha\beta} = \frac{\partial W(\lambda_r)}{\partial E_{\alpha\beta}} = \frac{\partial W}{\partial \lambda_1}\frac{\partial \lambda_1}{\partial E_{\alpha\beta}} + \frac{\partial W}{\partial \lambda_2}\frac{\partial \lambda_2}{\partial E_{\alpha\beta}} \tag{2.11}$$

Assuming a plane stress condition, the stress component $\mathbf{S}^{\alpha_3}$ vanishes. Subsequently, the principal stress values S_γ of the second Piola-Kirchhoff stress tensor are determined using the following equation (2.9) [2]:

$$S_\gamma = \lambda_\gamma^{-1}\frac{\partial W}{\partial \lambda_\gamma} = \lambda_\gamma^{-2}\sum_r \mu_r\left[\lambda_\gamma^{\alpha_r} - (\lambda_1\lambda_2)^{-\alpha_r}\right], (\gamma = 1,2,3) \tag{2.12}$$

The principal stretch values of the Cauchy stress tensor σ_γ are determined by the following equation:

$$\sigma_\gamma = \lambda_\gamma^2 S_\gamma = \sum_r \mu_r\left[\lambda_\gamma^{\alpha_r} - (\lambda_1\lambda_2)^{-\alpha_r}\right] \tag{2.13}$$

Thus, the stress $\mathbf{S}$ is determined as follows:

$$\mathbf{S} = \mathbf{T}^T\mathbf{S} \tag{2.14}$$

where:

$$\mathbf{S} = \begin{bmatrix} S^{11} & S^{12} \\ S^{12} & S^{22} \end{bmatrix}, \quad \mathbf{S} = \begin{bmatrix} S_1 \\ S_2 \\ 0 \end{bmatrix} \tag{2.15}$$

Equation (2.10) can also be derived by transforming the principal stresses:

$$\bar{\mathbf{S}} = \mathbf{R}\mathbf{S}\mathbf{R}^T \tag{2.16}$$

where:

$$\bar{\mathbf{S}} = \begin{bmatrix} S^{11} & S^{12} \\ S^{21} & S^{22} \end{bmatrix}, \quad \mathbf{R} = \begin{bmatrix} \cos\varphi & -\sin\varphi \\ \sin\varphi & \cos\varphi \end{bmatrix}, \quad \mathbf{S} = \begin{bmatrix} S_1 & 0 \\ 0 & S_2 \end{bmatrix} \tag{2.17}$$

For isotropic materials, the rotation angle φ is determined [2]:

$$\varphi = \frac{1}{2}\arctan\left(\frac{2g_{12}}{g_{11}-g_{22}}\right) \tag{2.18}$$

Substituting (2.17) into (2.16), the transformed stress (2.14) is obtained. For isotropic materials, the rotation angle φ from (2.14) is used, as $\mathbf{C}$ and $\bar{\mathbf{S}}$ share the same eigenvalues.

2.3.2 Linearization of the second Piola-Kirchhoff stress tensor

In this section, equation (2.14) will be linearized. Therefore, it is necessary to determine the derivative of $S_{\alpha\beta}$ with respect to $E_{\alpha\beta}$. The stiffness matrix $\mathbf{C_T}$ is defined as follows [2]:

$$\mathbf{C}_T = \mathbf{T}^T\,\bar{\mathbf{C}}\mathbf{T} = \begin{bmatrix} \frac{\partial S^{11}}{\partial E_{11}} & \frac{\partial S^{11}}{\partial E_{22}} & \frac{\partial S^{11}}{\partial (2E_{12})} \\ \frac{\partial S^{22}}{\partial E_{11}} & \frac{\partial S^{22}}{\partial E_{22}} & \frac{\partial S^{22}}{\partial (2E_{12})} \\ \frac{\partial S^{12}}{\partial E_{11}} & \frac{\partial S^{12}}{\partial E_{22}} & \frac{\partial S^{12}}{\partial (2E_{12})} \end{bmatrix} \tag{2.19}$$

where:

$$\bar{\mathbf{C}} = \begin{bmatrix} \frac{1}{\lambda_1}\frac{\partial S_1}{\partial \lambda_1} & \frac{1}{\lambda_2}\frac{\partial S_1}{\partial \lambda_2} & 0 \\ \frac{1}{\lambda_1}\frac{\partial S_2}{\partial \lambda_1} & \frac{1}{\lambda_2}\frac{\partial S_2}{\partial \lambda_2} & 0 \\ 0 & 0 & (S_1 - S_2)\left(\frac{\partial C_{12}}{\partial \varphi}\right)^{-1} \end{bmatrix} \tag{2.20}$$

So that:

$$\bar{\mathbf{C}} = \begin{bmatrix} \lambda_1^{-4}\left(\lambda_1\frac{\partial \sigma_1}{\partial \lambda_1} - 2\sigma_1\right) & \lambda_1^{-2}\lambda_2^{-2}\left(\lambda_2\frac{\partial \sigma_1}{\partial \lambda_2}\right) & 0 \\ \lambda_1^{-2}\lambda_2^{-2}\left(\lambda_1\frac{\partial \sigma_1}{\partial \lambda_2}\right) & \lambda_2^{-4}\left(\lambda_2\frac{\partial \sigma_2}{\partial \lambda_2} - 2\sigma_2\right) & 0 \\ 0 & 0 & \frac{(S_1 - S_2)\cos 2\varphi}{g_{11} - g_{12}} \end{bmatrix} \tag{2.21}$$

The derivatives of the Cauchy stresses $\boldsymbol{\sigma}_{\boldsymbol{\alpha}}$ from equation (2.13) are obtained as follows:

$$\begin{aligned} \lambda_1\frac{\partial \sigma_1}{\partial \lambda_1} &= \sum_r \mu_r \alpha_r \left[\lambda_1^{\alpha_r} - (\lambda_1\lambda_2)^{-\alpha_r}\right] \\ \lambda_2\frac{\partial \sigma_2}{\partial \lambda_2} &= \sum_r \mu_r \alpha_r \left[\lambda_2^{\alpha_r} - (\lambda_1\lambda_2)^{-\alpha_r}\right] \\ \lambda_2\frac{\partial \sigma_1}{\partial \lambda_2} &= \lambda_1\frac{\partial \sigma_2}{\partial \lambda_1} = \sum_r \mu_r \alpha_r (\lambda_1\lambda_2)^{-\alpha_r} \end{aligned} \tag{2.22}$$

Finally, the stiffness matrix $\mathbf{C}_T$ is determined for small deformations. The material parameters μ_r and α_r in their full form are given as follows:

$$\sum_r \mu_r \alpha_r = 2\mu \tag{2.23}$$

In which μ is the shear modulus. The component $\bar{C}_{33}(\lambda_\alpha = 1)$ is an indeterminate expression $\left(\bar{C}_{33}(\lambda_\alpha = 1) = \frac{0}{0}\right)$; however, it can be determined using the limit value:

$$\lim_{\lambda_\alpha \to 1} \frac{(S_1 - S_2)\cos 2\varphi}{g_{11} - g_{12}} = \mu \tag{2.24}$$

Using equations (2.23) and (2.24), the stiffness matrix $\mathbf{C}_T$ is determined according to Hooke's law for the behavior of incompressible materials:

$$\mathbf{C}_T(\lambda_\alpha = 1) = 2\mu \begin{bmatrix} 2 & 1 & 0 \\ 1 & 2 & 0 \\ 0 & 0 & 1/2 \end{bmatrix} = \frac{E}{1-\nu^2} \begin{bmatrix} 1 & \nu & 0 \\ \nu & 1 & 0 \\ 0 & 0 & \frac{1-\nu}{2} \end{bmatrix}_{\nu=0.5} \tag{2.25}$$

where $E = 2\mu(1+\nu)$ is Young's modulus, and ν is the Poisson's ratio.

2.3.3 Transformation of the equilibrium state equation

External forces are assumed to act on the surface of the thin membrane. The pressure constant p, defined as $p(x) = pn$, is considered per unit area of the deformed surface, acting in the direction of the vector $\mathbf{n}$ on the deformed membrane $\boldsymbol{\Omega}$. The formula for virtual work written for the deformed structure is represented in equation (2.22).

$$\int_{\Omega_0} S^T \delta E h_0 \, d\Omega_0 = \int_{\Omega} p n^T \delta x \, d\Omega \tag{2.26}$$

The virtual strain of the thin membrane $\delta E = \left[\delta E_{11}, \delta E_{22}, 2\delta E_{12}\right]^T$ is determined by the following equation:

$$\delta E_{\alpha\beta} = \frac{1}{2}\left(\delta u_{,\alpha} \cdot x_{,\beta} + x_{,\alpha} \cdot \delta u_{,\beta}\right) \tag{2.27}$$

Moreover, the unit vector $\mathbf{n}$, perpendicular to the deformed membrane, is determined by the normal vector of the tangent vectors $\mathbf{x}_{,\alpha}$ as follows:

$$\mathbf{n} = \frac{\mathbf{x}_{,1} \times \mathbf{x}_{,2}}{\| \mathbf{x}_{,1} \times \mathbf{x}_{,2} \|} \tag{2.28}$$

Therefore, the transformation of the current area element $d\Omega$ into the projected structure can be written as:

$$d\Omega = \frac{\| \mathbf{x}_{,1} \times \mathbf{x}_{,2} \|}{\| X_{,1} \times X_{,2} \|} d\Omega_0 \tag{2.29}$$

Substituting equations (2.28) and (2.29) into equation (2.26), the virtual work takes the form:

$$g(u, \delta u) = \int_{\Omega_0} \left[S^T \delta E h_0 - \frac{p}{\| X_{,1} \times X_{,2} \|} (\mathbf{x}_{,1} \times \mathbf{x}_{,2})^T \delta u \right] d\Omega_0 = 0 \tag{2.30}$$

Linearization is expressed as:

$$Dg(u, \delta u) = \int_{\Omega_0} \left[(\Delta S^T \delta E - S^T \Delta \delta E) h_0 - \frac{p}{\| X_{,1} \times X_{,2} \|} (\Delta x_{,1} \times x_{,2} + x_{,1} \times \Delta x_{,2})^T \delta u \right] d\Omega_0 = 0 \tag{2.31}$$

Linearization of the stress increment ΔS is presented in section 2.3.1, and the incremental virtual strain is given by the equation:

$$\Delta \delta E_{\alpha\beta} = \frac{1}{2} \left(\delta u_{,\alpha} \cdot \Delta u_{,\beta} + \Delta u_{,\alpha} \cdot \delta u_{,\beta} \right) \tag{2.32}$$

Equation (2.31) leads to the non-symmetric stiffness matrix in the finite element equation.

2.3.4 Finite element equation

In this section, the finite element equations of thin membrane theory, as presented earlier, will be described. Elements ranging from four to nine nodes are constructed using the displacement model. The initial geometric and displacement models are approximated using the same shape functions. With this method, arbitrarily curved surfaces can be discretized.

The following equations are formulated for a single element, $\mathbf{\Omega_e}$. Therefore, the position vector of the undeformed thin membrane and the displacement vector are approximated by mapping.

$$\mathbf{X}^h \big|_{\Omega_e} = \sum_{I=1}^{n_e} N_I \mathbf{X}_I \tag{2.33}$$

$$u^h \big|_{\Omega_e} = \sum_{I=1}^{n_e} N_I u_I \tag{2.34}$$

Therefore, the functions $N_I(\xi, \eta)$ are the shape functions corresponding to the nodal parameter I, where n_e represents the number of nodes for each element (ranging from 4 to 9 nodes). The terms X_I and u_I represent the nodal values of $\mathbf{X}^h$ and u^h in the element Ω_e, respectively. Thus, the position vector in the current state is given by:

$$\mathbf{x}^h \big|_{\Omega_e} = \mathbf{X}^h \big|_{\Omega_e} + u^h \big|_{\Omega_e} \tag{2.35}$$

The finite element approximation of the virtual strain is expressed as:

$$\delta E^h = \sum_{I=1}^{n_e} \mathbf{B}_I \delta u_I, \quad \mathbf{B}_I = \begin{bmatrix} N^h_{I,1} x_1^{hT} \\ N^h_{I,2} x_2^{hT} \\ N^h_{I,1} x_2^{hT} + N^h_{I,2} x_1^{hT} \end{bmatrix} \tag{2.36}$$

Using the approximations for displacements (2.29) and for virtual strain (2.30), the weak form of the equilibrium state (2.26) is established:

$$g_e(u, \delta u) = \sum_{I=1}^{n_e} \delta u_I^T \int_{\Omega_e} \left[\mathbf{B}_I^T \mathbf{S}^T h_0 - p \frac{\mathbf{x}^h_{,1} \times \mathbf{x}^h_{,2}}{\| \mathbf{X}_{,1} \times \mathbf{X}_{,2} \|} N_I \right] d\Omega_e = 0 \tag{2.37}$$

The stress vector $\mathbf{S}^h$ is determined using the finite element approximation of the material law represented in equation (2.14).

The nonlinear finite element equation is solved using the Newton-Raphson method. Therefore, the finite element approximation of the weak form must be evaluated for each iteration.

$$Dg_e(u, \delta u)\Delta u = \sum_{I=1}^{n_e} \sum_{K=1}^{n_e} \delta u_I^T \mathbf{K}_{IK} \Delta u_K \tag{2.38}$$

In equation (2.38), K_{IK} is the tangent stiffness matrix for a single element node, defined as:

$$K_{IK} = \int_{\Omega_e} \left[(\mathbf{B}_I^T \mathbf{C}_T \mathbf{B}_K + G_{IK}) h_0 - P_{IK} \right] d\Omega_e \tag{2.39}$$

The material stiffness matrix $\mathbf{C}_T$ is described in equation (2.19), and the geometric matrix G_{IK} is derived from equation (2.32) as follows:

$$G_{IK} = diag\left[g_{IK}, g_{IK}, g_{IK} \right] \tag{2.40}$$

Here, g_{IK} is defined as:

$$g_{IK} = S^{11} N_{I,1} N_{K,1} + S^{22} N_{I,2} N_{K,2} + S^{12} (N_{I,1} N_{K,2} + N_{I,2} N_{K,1})$$

Lastly, the linearization of the external force load results in the skew-symmetric matrix P_{IK}:

$$P_{IK} = \frac{p}{\| \mathbf{X}^h_{,1} \times \mathbf{X}^h_{,2} \|} \begin{bmatrix} 0 & -p^3_{IK} & p^2_{IK} \\ -p^3_{IK} & 0 & -p^1_{IK} \\ p^2_{IK} & -p^1_{IK} & 0 \end{bmatrix} \tag{2.41}$$

where: $p^n_{IK} = (x^h_{,1} N_{I,2} - x^h_{,2} N_{I,1}) N_K, (n = 1,2,3)$.

In the final part of this section, the computation of the derivatives of the shape functions $N_{I,\alpha}$ is described. This is useful for introducing the local coordinate system t_i $(i = 1,2,3)$ associated with the coordinates s_i in the undeformed state for each element. In cases where the components of the stress tensor and strain tensor are mutually dependent, the chain rule

is applied. The derivatives of the shape functions $\partial N_I / \partial s_\alpha = N_{1,\alpha}$ $(\alpha = 1,2)$ are defined as follows:

$$\begin{bmatrix} N_{I,1} \\ N_{I,2} \end{bmatrix} = J^{-1} \begin{bmatrix} N_{I,\xi} \\ N_{I,\eta} \end{bmatrix}, \quad J = \begin{bmatrix} \frac{\partial s_1}{\partial \xi} & \frac{\partial s_2}{\partial \xi} \\ \frac{\partial s_1}{\partial \eta} & \frac{\partial s_2}{\partial \eta} \end{bmatrix} \tag{2.42}$$

To complete the process, the Jacobian transformation matrix J must be evaluated. The tangent vectors are calculated by taking the partial derivatives of the position vector of the undeformed geometry $X(\xi,\eta)$ with respect to the coordinates ξ and η:

$$G_1 = \frac{\partial X}{\partial \xi}, \quad G_2 = \frac{\partial X}{\partial \eta} \tag{2.43}$$

The vectors G_1 and G_2 are not necessarily unit vectors and may not be orthogonal. However, the local orthogonal coordinate system t_i can be computed as follows:

$$t_n = \frac{G_1 \times G_2}{\| G_1 \times G_2 \|}, \quad t_1 = \frac{G_1}{\| G_1 \|}, \quad t_2 = t_n \times t_1 \tag{2.44}$$

Using equations (2.39) and (2.40), the components of the Jacobian matrix $J_{\alpha\beta} = G_\alpha \cdot t_\beta$ $(\alpha,\beta = 1,2)$ are determined. Finally, the area element $d\Omega_e$ is transformed using the following relation:

$$d\Omega_e = \left\| \frac{\partial X}{\partial \xi} \times \frac{\partial X}{\partial \eta} \right\| d\xi d\eta \tag{2.45}$$

This is then substituted into equations (2.37) and (2.39). The tangent stiffness matrix and the load vector components are calculated using Gaussian quadrature. Each component is assembled into the global equation using a standard procedure.

2.4 Human skin electromagnetic response

The human skin is considered a complex organ, necessitating certain simplifications when modelling its electromagnetic behaviour, given the inherent differences between biological tissues and classical electromagnetic models [14]. In an electromagnetic model, the clear definition of all sources, including charges, currents, voltages, and modes of electromagnetic wave excitation, is required. Specifically, high-frequency currents in ducts, which may result from proton hopping, are considered, while ionic flows producing currents at lower frequencies are excluded from the simulation model due to their negligible impact. The differences in electric potential within the skin may arise from pH gradients or

variations in membrane potential. To achieve accurate simulation, an idealized section of the skin is constructed, with materials in various subdomains categorized distinctly based on their electrical properties.

The propagation of electromagnetic waves through an inhomogeneous medium is typically described using a 4 × 4 polarization scattering matrix. This matrix characterizes the interaction of monochromatic plane waves, accounting for both orthogonal polarizations involved in the scattering process. Each element of the matrix represents the coupling between the incident and scattered wave components, providing a comprehensive description of how the wave's polarization state is altered upon interaction with the medium. However, in scenarios where the incident and scattered waves maintain the same polarization (i.e., the source and receiver share identical polarization states), $S(\omega)$, where $\omega = 2\pi f$ and f is denotes the wave frequency. This simplified matrix captures the essential scattering characteristics for single-polarization systems [15].

$$S(\omega) = \begin{pmatrix} S_{11}(\omega) & S_{12}(\omega) \\ S_{21}(\omega) & S_{22}(\omega) \end{pmatrix} \tag{2.46}$$

Here, the element $S_{11}(\omega)$ represents the reflection coefficient, defined as the ratio of the complex magnitudes of the reflected plane wave, $U_{\text{ref}}(\omega)$, to the incident plane wave, $U_{\text{in}}(\omega)$:

$$S_{11}(\omega) = \frac{U_{ref}(\omega)}{U_{in}(\omega)} \tag{2.47}$$

Similarly, the element $S_{21}(\omega)$ is the propagation coefficient, defined as the ratio of the complex magnitudes of the propagated plane wave, $U_{\text{prop}}(\omega)$, to the incident plane wave, $U_{\text{in}}(\omega)$:

$$S_{21}(\omega) = \frac{U_{prop}(\omega)}{U_{in}(\omega)} \tag{2.48}$$

Several mixture formulas are used to calculate the bulk dielectric response of binary systems. When domain boundary effects are disregarded, the applicable formula typically lies between two extremes: one assuming separate layers (extreme anisotropy) and the other assuming a spatially uniform distribution of spheres within a dielectric medium, as modelled by the Maxwell–Wagner approach. However, within the frequency range of interest, the dielectric properties of water and the dry components of skin show minimal

differences between these two extremes. Specifically, the variation in the real part of the complex permittivity is less than 0.1. Consequently, the Maxwell–Wagner equation can be applied to accurately determine the permittivity of the mixtures [16]:

$$\varepsilon_{mix} = \varepsilon^{bm} \frac{(2\varepsilon^{bm} + \varepsilon^{w}) - 2\phi(\varepsilon^{bm} - \varepsilon^{w})}{(2\varepsilon^{bm} + \varepsilon^{w}) + \phi(\varepsilon^{bm} - e^{w})} \tag{2.49}$$

where ε^{bm} represents the permittivity of the dry biological structural components, ε^{w} is the permittivity of water, and ϕ denotes the volume fraction of the water component.

The complex permittivity $\varepsilon^{w}(\omega)$ of bulk water in the extremely high frequency (EHF) band is widely recognized to be accurately modeled using the Cole–Cole relationship:

$$\varepsilon^{w}(\omega) = \varepsilon_{\infty} + \frac{\varepsilon_S - \varepsilon_{\infty}}{1 + (i\omega\tau_0)^{1-\alpha}} \tag{2.50}$$

where ε_{∞} is the high-frequency permittivity, ε_S is the static permittivity, τ_0 is the relaxation time of the process, and α is the broadening parameter.

The specific absorption rate (SAR) represents the power density of electromagnetic energy dissipated in biological tissue [17]. SAR can be reported as a whole-body average or, more commonly, as a spatially averaged value within a defined mass—typically 1 g (local SAR) or 10 g (10-g averaged SAR) of tissue. Because SAR depends on the local electric-field intensity inside the dielectric medium that models human tissue, it is quantitatively determined from the electric-field distribution using equation (2.51):

$$SAR = \frac{\sigma}{\rho}|E|^2 \quad [W/Kg] \tag{2.51}$$

here, E denotes the local electric-field magnitude ($V.m^{-1}$), σ the tissue conductivity ($S.m^{-1}$), and ρ the mass density ($kg.m^{-3}$). Because each of these quantities varies with the intrinsic dielectric properties of biological tissue, the human body is usually represented as a stratified medium. For greater anatomical fidelity, most studies subdivide the tissue into five or six discrete layers.

For a homogeneous medium, the depth-wise (z-axis) profile of the specific absorption rate (SAR) exhibits a simple exponential attenuation. Hence the volumetric SAR can be decomposed into an in-plane component and a depth-dependent decay term, as expressed in equation (2.51). Here, SAR (x, y, z_s) denotes the SAR evaluated in the x–y plane at a depth $z = z_s$ beneath the skin surface, while the characteristic penetration depth is given by $\delta = -10.7 f_{GHz} + 40.4$ with δ in millimetres:

$$SAR(x,y,z) = SAR(x,y,z_s)e^{\frac{-2(z-z_s)}{\delta}} \tag{2.52}$$

The volume-averaged specific absorption rate SAR_v, for an organ of volume v is obtained by integrating the spatial SAR distribution given in equation (2.51) over the entire organ domain, leading to the expression summarized in equation (2.52):

$$SAR_v = \frac{1}{V_{tot}} \iint dxdySAR(x,y,z_s)\frac{\delta}{2}e^{\frac{2z_s}{\delta}}(1-e^{\frac{2z}{\delta}}) \tag{2.53}$$

2.5 Analysis Systems (ANSYS) and finite element model for human skin

2.5.1 Briefly about ANSYS and applications in biomechanics

Ansys, Inc. is an American multinational company with its headquarters based in Canonsburg, Pennsylvania. It develops and markets CAE/multiphysics engineering simulation software for product design, testing and operation and offers its products and services to customers worldwide [18].

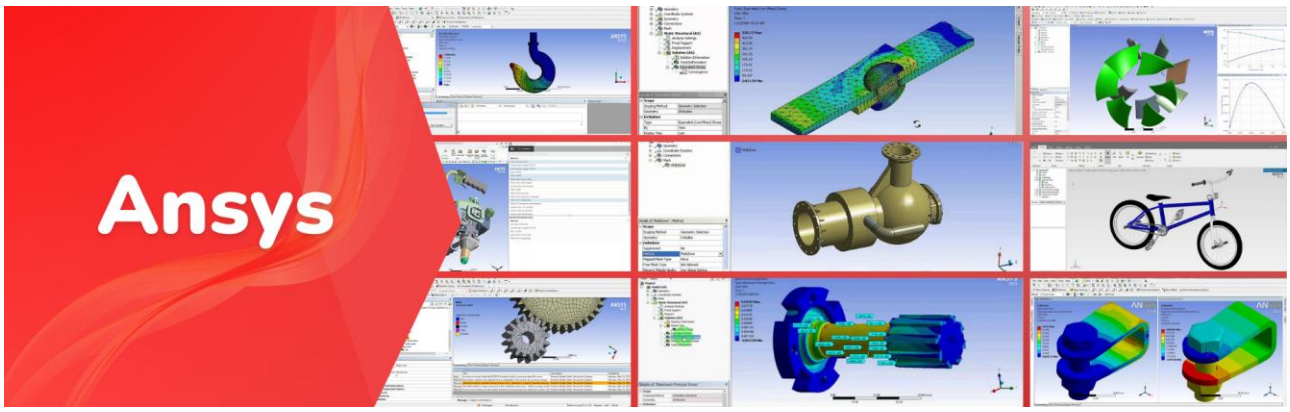

Figure 2.4 Ansys software provides a graphical user interface (GUI) for simulating various subjects, including in biomechanics field

Ansys simulation software, with its comprehensive Multiphysics capabilities, provides bundles that offer structural mechanics, explicit dynamics, fluid dynamics and thermal simulation capabilities. These bundles also include Ansys Workbench, relevant CAD import tools, solid modeling and meshing, and high-performance computing (HPC) capability. Electronics Academic Products: Bundles that offer high-frequency, signal integrity, RF, microwave, millimeter-wave device and other electronic engineering simulation

capabilities. These bundles include products such as Ansys HFSS, Ansys Q3D Extractor, Ansys Slwave, Ansys Maxwell and Ansys Simplorer Advanced.

In biomechanics, Ansys is widely used to simulate and analyze the mechanical behavior of biological systems and medical devices [19]. Applications include the design of orthopedic implants, cardiovascular devices, and dental prosthetics, where simulations assess stress distribution, fluid dynamics, and material compatibility. For instance, CFD tools in Ansys help optimize blood flow in stents and artificial heart valves, while FEA aids in understanding bone fracture healing under varying mechanical loads. By enabling accurate modeling of complex geometries and coupled physical phenomena, Ansys enhances the safety, performance, and efficiency of medical devices, contributing significantly to advancements in biomedical engineering.

2.5.2 The development of finite element model for human skin

The development of computational models for human skin began in the 1970s. At that time, human skin was modeled as a thin membrane with hyperelastic properties. However, due to technological limitations and the lack of simulation tools, mathematical equations were the primary approach used to analyze skin deformation.

Today, with advancements in computer technology and finite element (FE) software, simulations of skin deformation have become feasible. For instance, finite element formulations have been proposed for thin rubber membranes [2]; human tissue deformation analysis and nonlinear FEM using Ansys were presented in [20]; in [21], ABAQUS was used as a tool to simulate the intubation process; additionally, MRC MARC was chosen to simulate suction experiments on skin.

In this study, a finite element (FE) model for human skin is utilized and simulated using Ansys software. Two case studies are investigated using two types of elements: the PLAN183 element and the SOLID186 element.

2.5.2.1 2D model: PLANE183 element

For the case of a 2D model of human skin, the PLANE183 element is used. PLANE183 is a higher-order 2D element, defined by either 8 or 6 nodes. This element features a quadratic shape function, making it suitable for modeling complex geometries and nonlinear behaviors. The shape, nodal positions, and coordinate system of the PLANE183 element are illustrated in Figure.

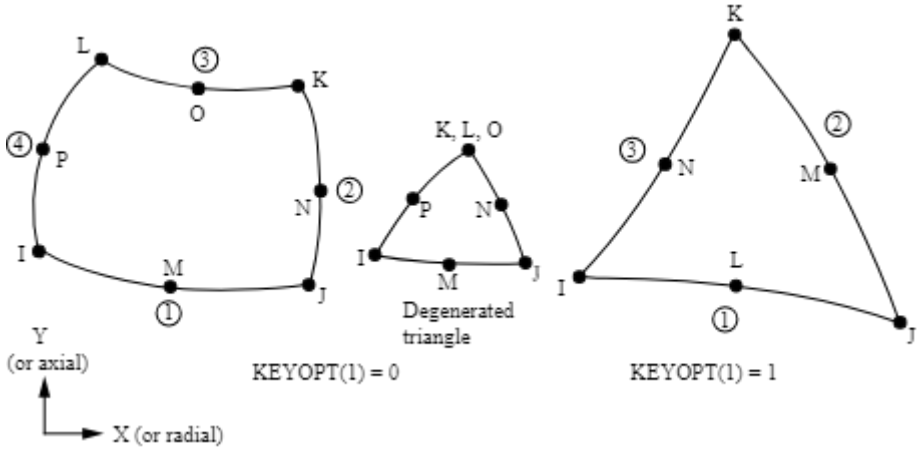

Figure 2.5 PLANE183 element (the geometry, node locations, and the coordinate system)

This element can be used for planar models (plane stress, plane strain, or generalized plane deformation) or for axisymmetric problems (with or without torsion). It can incorporate material properties such as plasticity, hyperelasticity, creep, hardening, large deflection, and large strain. In most cases, the element has two degrees of freedom per node: translations in the X and Y directions. However, in cases of asymmetric torsion, the element features three degrees of freedom per node: translations in the X and Y directions, and rotation about the Y-axis. Additionally, the element supports a mixed formulation, allowing it to simulate incompressible or fully incompressible hyperelastic materials.

The input data for the element includes the thickness (applicable only for plane stress conditions) and material properties for orthotropic materials (if applicable). The directions of the orthotropic material properties align with the directions of the element. Input pressures can be defined as surface loads acting on the element's surface. Concentrated forces should be specified as forces per unit depth for plane analysis and based on a 360° symmetry assumption for axisymmetric structural analysis. The solution output associated with the element is nodal displacements included in the overall nodal solution, is demonstrated in Figure 2.4.

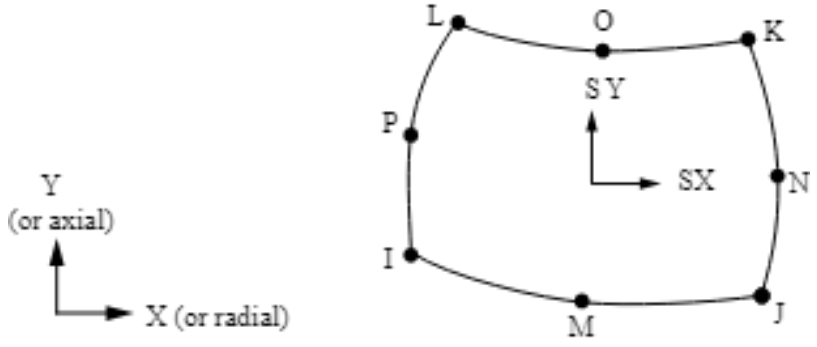

Figure 2.6 PLANE183 element stress output

2.5.2.2 3D model: SOLID186 element

For the case of 3D modeling of human skin, the SOLID186 element is used. SOLID186 is a higher-order 3D solid element with 20 nodes, capable of representing second-order displacement behavior. Each node has three degrees of freedom: translations in the X, Y, and Z directions. Additionally, this element can simulate material properties such as plasticity, elasticity, creep, stress hardening, large deflection, and significant large strain. The shape, nodal positions, and coordinate system of the SOLID186 element are illustrated in Figure 3.1b. Similar to the PLAN183 element, this element also supports a mixed formulation to simulate incompressible and fully incompressible hyperelastic materials.

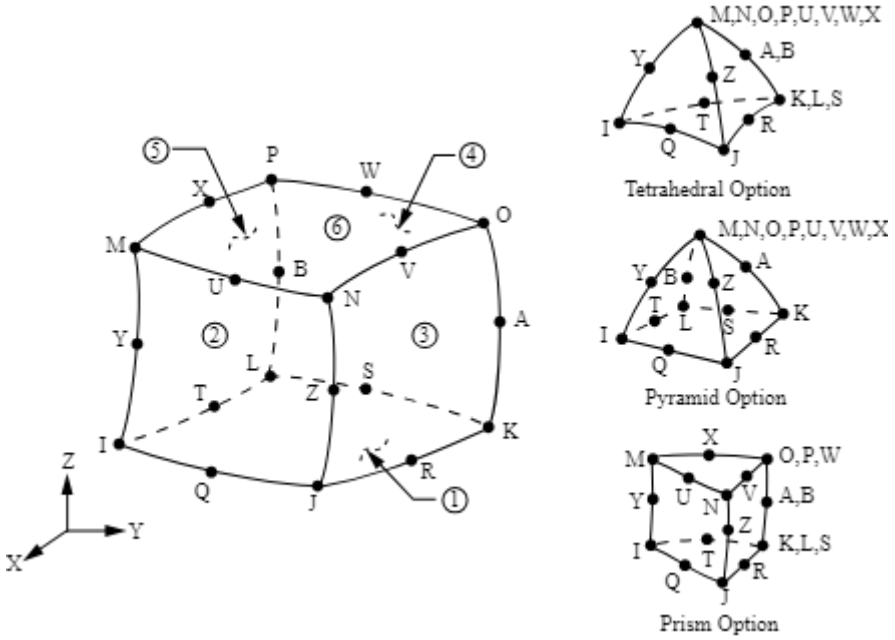

Figure 2.7 SOLID186 element homogeneous structural solid geometry

The SOLID186 element has two configurations: a homogeneous solid structure and a layered solid structure. Within the scope of this study, the homogeneous solid structure configuration is applied to the human skin model.

The homogeneous solid structure is well-suited for modeling irregular meshes. The elements can be arbitrarily oriented in space. Apart from the nodes, the input data includes anisotropic material properties. The directions of the anisotropic materials correspond to the element directions. Input pressures can be defined as surface loads acting on the element's surfaces.

The SOLID186 element employs two integration methods: the "reduced integration" method and the "full integration" method, described as follows:

- Reduced Integration Method: This method helps mitigate "volume locking" when dealing with nearly incompressible materials. However, the "hourglass" mode may propagate through the model if there are not at least two layers of elements in each direction.
- Full Integration Method: This method does not induce the "hourglass" mode but may lead to "volume locking" when materials are nearly incompressible. It is mainly used for purely linear analyses or when the model consists of only a single layer of elements in each direction.

One of the challenges of this study is to simulate and compare the results with the reference [22]. Therefore, the finite element model must be carefully constructed to achieve minimal error.

CHAPTER 3: METHODOLOGY

3.1 Information and experimental data from previous studies

As discussed in Chapter 1, understanding the behavior of human skin requires an accurate simulation model or precise mechanical properties. To achieve reliable results, the "Motion Capture" system has been applied in experimental methods to determine the displacement of living human skin [23], a system developed by Mahmud [24, 25].

The results obtained from these systems are considered reliable and valuable. Experimental data can be used to analyze deformation properties, anisotropy, and the nonlinear characteristics of the skin. However, these results do not directly provide the mechanical properties of human skin. Therefore, the characteristics of the skin must be determined through numerical simulation methods, specifically finite element analysis (FEA), to serve as a basis for analyzing skin deformation in future studies. Simulation results will be compared with experimental data, although, to date, no universally accepted model for human skin exists.

In this thesis, the experimental data, Ogden material parameters, and boundary conditions are referenced from prior studies [2, 22]. Based on this data, a simplified human skin model is constructed, and the simulation results are compared against experimental data. The data used to develop the human skin model is referenced from Jamaluddin Mahmud et al. [23]. In their study, an “In vivo Skin Deformation Motion” experiment was conducted on the elbow skin of healthy volunteers aged between 23 and 42 years, with an average age of 28 years. A set of reflective markers was attached to the skin on the elbow of the volunteers. Skin deformation was induced by applying a tensile force using a nylon thread attached to the midpoint of the markers. The markers, labeled from P1 to P9, were aligned in parallel and in a straight line with the applied load, where P5 served as the load application point. The other end of the nylon thread was connected to a force sensor.

The Qualisys Proflex – MCU1000 system, equipped with three optical cameras and 50 mm focal length lenses, was used to record and track skin deformation. Researchers marked experimental points on films of various sizes and shapes to ensure camera accuracy. Optimizing the cameras' position and angles enhanced both accuracy and resolution. High precision, with an average residual error of approximately 0.05 mm, was achieved through static calibration using diamond-shaped markers measuring 3 × 2 mm.

Before conducting the experiment, a reliable, meticulous, and efficient experimental method was developed. Since the system measures small-scale areas (80 mm × 60 mm), placing the markers too close together resulted in overlapping markers. Conversely, markers spaced too far apart led to the loss of critical information between them. After several trials, the number of markers was optimized to 42, with an 8 mm spacing, ensuring suitability and effectiveness for human skin.

The experimental data obtained from the "In vivo Skin Deformation Motion" experiment was used to develop and simulate the skin model using the finite element method (FEM). Subsequently, the Ogden material parameters were verified.

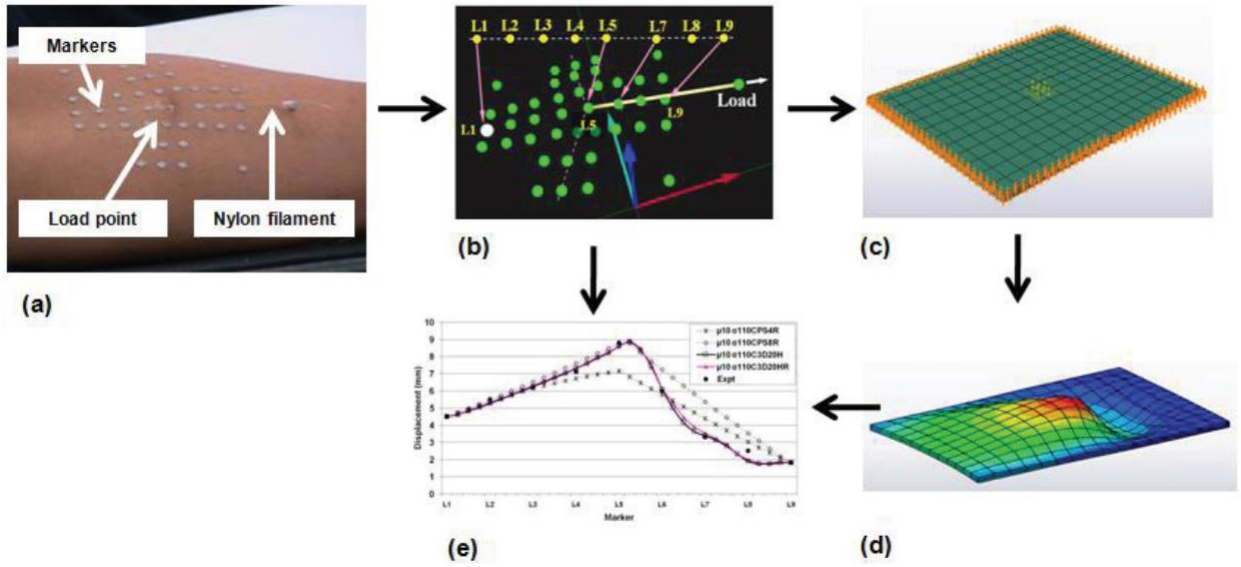

Figure 3.1 Integration of motion capture-marker tracking-FE modelling simulation to quantify skin parameters (a) inducing skin deformation by pulling a nylon filament stuck at the centre of the marker set, (b) sample output from the tracking software showing the markers' label and movement, (c) 80 x 60 mm plate, meshed into 384 (16 x 12 x 2) brick quadratic elements, the yellow arrows indicate the distributed load applied, (d) simulation, and (e) comparison of results

Over the past four decades, FEA has been widely regarded as the preferred method in computational biomechanics. However, conventional approaches for soft tissue deformation largely rely on linear finite element algorithms, which operate under the assumption of infinitesimal deformations. This assumption is incompatible with the nature of soft tissue modeling for surgical simulations and image-guided surgeries, where the problem involves large deformations and strains, along with geometric and material non-linearities.

Another study by author Thach Song Ngoc Dinh et al. [26] investigated the Ogden material parameters of order 2. Along with an experimental study, the authors developed to determine the appropriate parameters to match the mechanical behavior of the skin. The results of the author's group showed that the suitable parameter pair for order 2 is (μ = 10 Pa, α = 120) for the SOLID186 element. Under the same conditions as previous experiments, the results showed a bow wave effect and were close to the results of Jamaluddin Mahmud [22, 23].

Co-rotational finite elements were introduced to enable near real-time computation of deformations. Despite this advancement, they are limited by the assumption of small strains, which fails to meet the requirements of many clinically relevant scenarios. Another challenge in applying Finite Element Method (FEM) to patient-specific applications is the frequent use of 4-noded tetrahedral elements, which are prone to volumetric locking and are unsuitable for modeling nearly incompressible materials like soft tissues. While parabolic 10-noded tetrahedral elements address this issue, they are computationally inefficient. In contrast, 8-noded hexahedral elements are more efficient, but the generation of hexahedral meshes for complex geometries remains a significant challenge despite extensive research efforts. Simulating needle insertion presents even greater challenges for FEM. Very large strains occur at the needle tip, with studies reporting strains of up to 80% near the tip during insertion into swine brain tissue. These extreme deformations result in element distortion, necessitating remeshing and further complicating the simulation process.

3.2 Computational model in simulation 1

The modeled object is a thin square plate with dimensions of 80 x 60mm in Figure 3.2. Additionally, to determine the displacements at points P_n $(n = 1, 2, 3, ..., 9)$, the flat plate model is also marked with the corresponding points P_n. The selection of boundary conditions and the Ogden material parameters will be further detailed in Chapter 4. The simulation scenario is configured with the default assumption of normal human body temperature, set at 36°C.

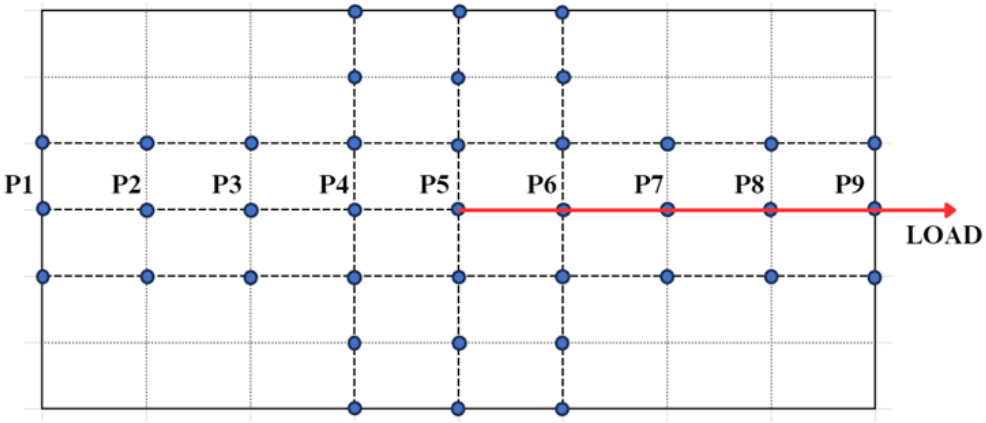

Figure 3.2 The thin plate model was constructed using Ansys

3.3 Computational model in simulation 2

Conductivity is a key parameter in understanding how skin interacts with electromagnetic fields, particularly in medical applications such as diagnostic imaging, therapeutic treatments, and the assessment of exposure to electromagnetic radiation. The electrical conductivity of human skin varies widely across its layers, reflecting the different structural and compositional characteristics of each layer. The direct current (DC) conductivity of the dermis, epidermis, and hypodermis has been reported as approximately 0.2 S/m, 0.025 S/m, and 10-5 S/m, respectively [27]. However, the effective conductivity of the dermis and epidermis at higher frequencies is observed to be significantly greater. Given that the conductivity of blood at 100 GHz is measured to be approximately 60 S/m, the high-frequency conductivity of the dermis is estimated to be around 40 S/m. Additionally, the conductivity of the epidermis, which contains a negligible amount of blood vessels and has a lower water content than the dermis, is approximated at 1 S/m at 100 GHz. In contrast, the hypodermis, being composed of dry, dead cellular material, is characterized by minimal conductivity [28].

Table 3.1 The conductivity parameters of the human skin layers

Layer	DC conductivity (S/m)	AC conductivity (S/m)	Permittivity	Layer width (μm)
Dermis	0.1	30	3.9	1000
Epidermis	0.01	1	3.2	350
Hypodermis	10^{-5}	10^{-5}	2.4	30

Due to the limitations in research facilities, the simulation model for this study will be simplified by simulating a rectangular microwave cavity (50mm x 50mm x 40mm) with a wave port (20mm x 10mm x 5mm). After setting up the cavity model, the research team constructed three rectangular blocks representing the three basic layers of human skin, with the basic material parameters as outlined in Table 3.1.

The surfaces of the cavity will be applied with Finite Conductivity boundary conditions [29]. This boundary condition is particularly effective for modelling metal structures that are thin yet exceed the skin depth in thickness. It is applicable for simulating signal traces, ground planes, and radiating elements, enabling precise control over the surface roughness of the conducting material. The boundary condition is applied to a sheet object that, while drawn as a 2D object, accurately represents the characteristics of a 3D conductor in the simulation. An excitation will be applied to the input surface of the wave port to define the microwave radiation input.

$$E_{\tan} = Z(n \times H_{\tan}) \tag{3.1}$$

where: E_{tan} represents the tangential component of the electric field on the surface. Htan represents the tangential component of the magnetic field on the surface. Z_s is the surface impedance of the boundary. When the layer thickness significantly exceeds the skin depth, Z_s can be approximated using (1 + j)/(ds). However, if this condition is not met, Z_s is calculated using the transmission line model, as applied in the layer impedance boundary condition.

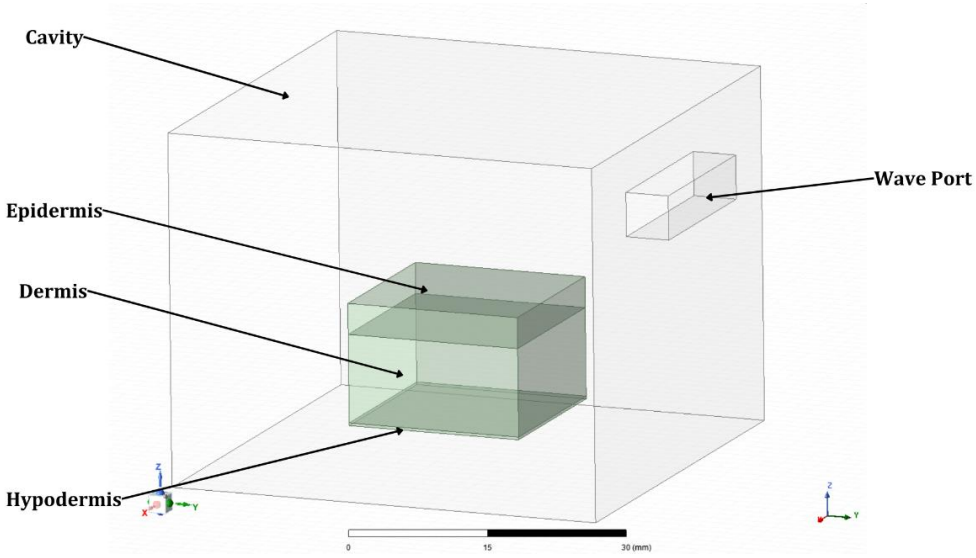

Fig 3.3 The simulation of microwave cavity with the model of human skin layers inside

CHAPTER 4: FINITE ELEMENT ANALYSIS FOR HUMAN SKIN

4.1 Validation of the numerical computational model

This section will present the validation problem of the simulation model using the ANSYS Workbench program. A rectangular plate with a circular hole at the center is investigated. Due to symmetry, only ¼ of the model is analyzed to save computational costs. The dimensions of the plate are $L = 10mm$, the radius $R = 3mm$, and the thickness $h = 1mm$. The model is meshed with 2551 nodes and 812 quadrilateral elements. A uniform tensile force, $q = 90N$, is applied to the right edge, and symmetry boundary conditions are applied to the left (DC) and bottom (BA) edges. The problem is depicted in Figure 4.1.

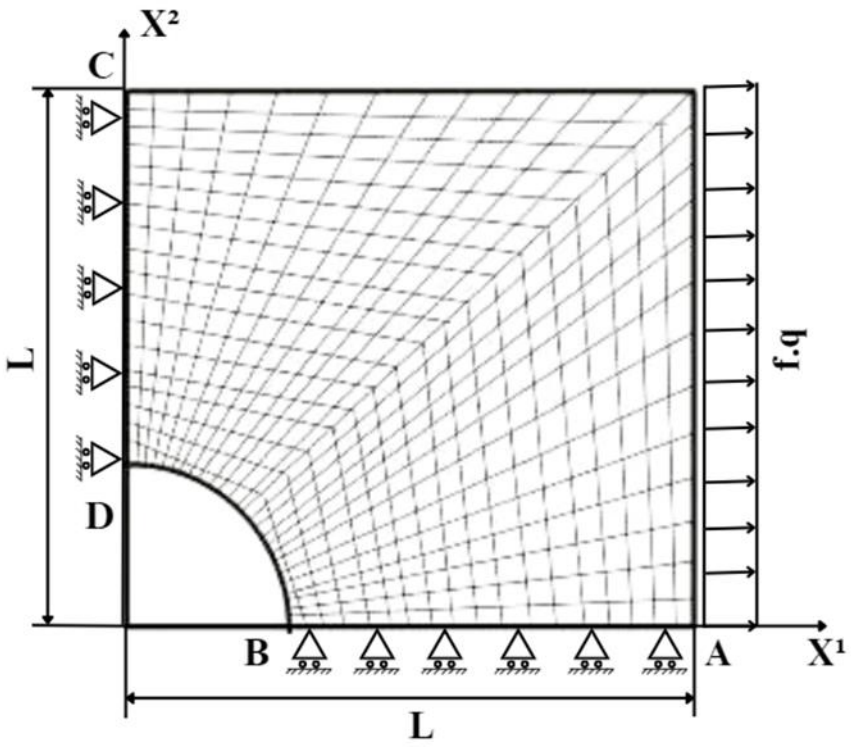

Figure 4.1 The finite element model for the validation problem needs to be verified

To demonstrate that using the Ogden hyperelastic material is a viable choice, the problem was studied and validated by Thach Song Ngoc Dinh [1] through a comparison of results for the second-order Ogden material with reference data [2]. The displacement results were compared with those obtained from the finite element model conducted using the ABAQUS software [2] to verify the proposed approach in this thesis. Thus, the use of the Ogden material model with the ANSYS Workbench program produced results consistent with the reference solutions, supporting the development of a finite element model for human skin.

4.2 Development of a finite element model for human skin simulation

Based on the information from Sections 2.5 and 3.1, skin simulations were performed to validate the finite element model for nonlinear skin analysis. The computational models were created with the assistance of ANSYS Workbench. A simplified skin model was simulated as a rectangular flat plate with dimensions of 80 mm x 60 mm. The deformation results were compared with experimental data provided by Jamaluddin Mahmud et al. [22].

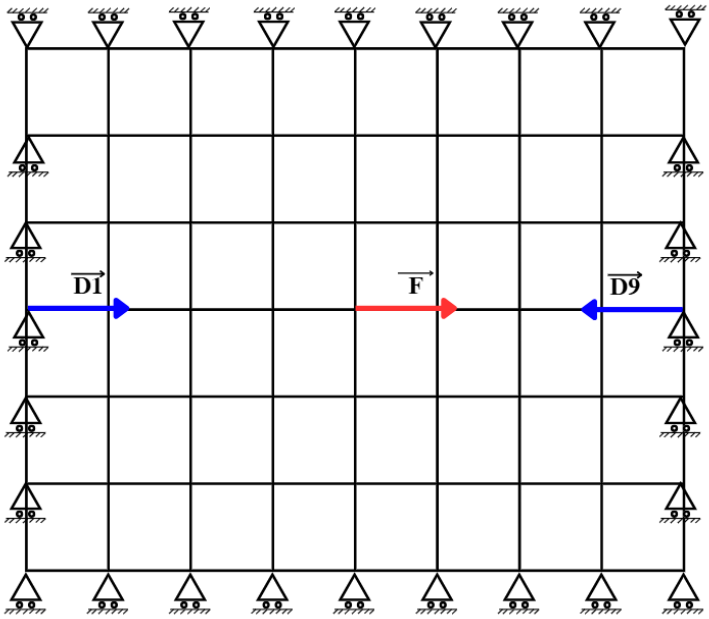

Figure 4.2 Loading and boundary conditions of the finite element model of the human skin

In this study, the skin model is considered as a nonlinear hyperelastic material, with assumptions derived from Tong and Fung [30], Evan [31], and Ogden's model has yielded good results. The purpose of this experiment is to investigate the influence of the third axis (Z-axis) and evaluate the material parameters of Ogden when used to accurately describe the behavior of human skin. In reality, the 2D skin model cannot match the actual behavior of human skin, and the displacement results show significant errors. Therefore, a 3D model needs to be defined to accurately describe the behavior of human skin. Besides that, the parameters of the hyperelastic model that we apply are demonstrated in Table 4.1.

4.3 Loads and boundary conditions

For the nonlinear skin model analysis, skin simulation was conducted to verify the finite element model based on the theory of hyperelastic materials using Ogden's model and the finite element method. The computational models were created with the assistance of ANSYS Workbench. Boundary conditions and loads are depicted in Figure 4.2. A load of F

= 10N was applied at point P_5 of the skin model and parallel to the other midpoint points. Symbols D_1 and D_9 represent displacement boundary conditions at points P_1 and P_9.

Before experimenting, a reliable, meticulous, and efficient experimental method was developed. Due to the system handling measurements on a small scale (80 mm x 60 mm), placing markers close to each other led to marker overlap. Conversely, spacing markers too far apart would result in missing information between them. Therefore, after several trials, the optimal number of markers was determined to be 42 (spaced 8 mm apart), which was applied effectively and efficiently on human skin. Experimental data from the "In vivo Skin Deformation Motion" experiment [23] were used to develop and simulate the skin model using the finite element method. Figure 4.3 shows how the markers placed in the forearm with the model node illustrate how the load will take. Subsequently, the material parameters of Ogden were validated in Table 4.1.

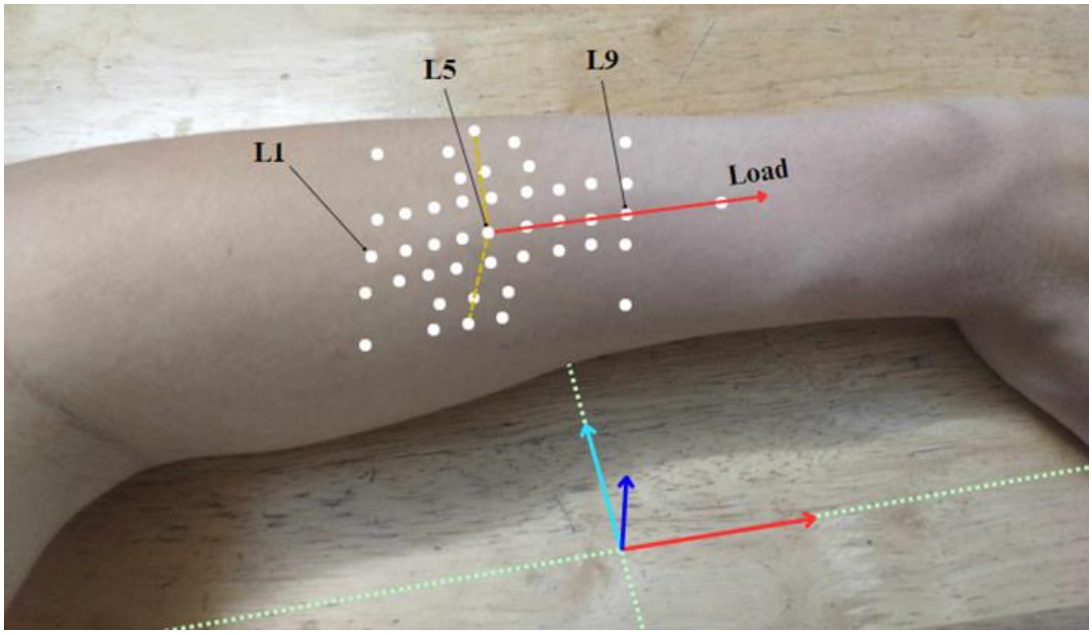

Figure 4.3 The experiment simulates skin deformation by pulling a nylon thread attached at the center point, as shown in the figure, indicating the contact points and pulling directions on the human skin

4.4 Material parameter selection

To enhance the accuracy of Ogden hyperelastic material simulations and align them more closely with real-world experimental models, Ogden material parameters for the first-order, second-order, and third-order models are compared. This comparison ensures that the chosen model closely represents experimental observations. Each order exhibits different

degrees of equivalence, as higher-order models tend to oversimplify the stress-energy curve, leading to less realistic outcomes. Previous studies have demonstrated that the second-order Ogden model aligns most accurately with biological tissues. Below is a Table 4.1 that summarizes the simulations conducted to evaluate the correlation between the proposed 2D model and the experimental data.

These values correspond to an initial Young's modulus for small strains of 0.99 MPa for Shergold and Fleck, and 0.00026 MPa for the results presented here, which represents a significant difference. It is evident that skin properties vary greatly; potential reasons for this include the fact that Jansen and Rottier used skin from the lower abdomen, and cadaveric skin tested under non-physiological conditions is likely to exhibit different behavior. Clearly, a more comprehensive testing program across different individuals and body areas is needed to better understand this variation. The method presented here offers a possible approach for conducting such a study.

Table 4.1 The parameters of Ogden 3rd model in engineering data in ANSYS Workbench

Property	**Value**	**Unit**
Material constant MU1	0.69	MPa
Material constant A1	1.3	-
Material constant MU2	0.01	MPa
Material constant A2	4	-
Material constant MU3	-0.0122	MPa
Material constant A3	-2	-
Incompressibility Parameter D1	0.1	MPa^{-1}
Incompressibility Parameter D2	0.1	MPa^{-1}
Incompressibility Parameter D3	0.1	MPa^{-1}

4.5 Simulation results validating material parameters

4.5.1 Case 1: 2D human skin model

4.5.1.1 2D model with a coarse element mesh

The skin model is meshed with 48 second-order 8-node elements (8 × 6 elements). The load and boundary conditions are discussed in Section 4.3. The PLANE183 element and six sets of Ogden material parameters (μ = 10 Pa, α = 40; μ = 10 Pa, α = 50; μ = 10 Pa, α = 90; μ = 10 Pa, α = 100; μ = 10 Pa, α = 110; μ = 10 Pa, α = 120) are analyzed.

Table 4.2 The parameters and experiments of the hyperelastic model

Number of experiments	Parameter	Value	Unit
Test 1	μ	10	Pa
	α	40	-
Test 2	μ	10	Pa
	α	50	-
Test 3	μ	10	Pa
	α	90	-
Test 4	μ	10	Pa
	α	100	-
Test 5	μ	10	Pa
	α	110	-
Test 6	μ	10	Pa
	α	120	-

The horizontal axis represents the marker positions, while the vertical axis shows the displacements (in mm). The black line represents the experimental data, and the colored lines represent the simulation results for different parameter sets. The simulation results for α = 110 and α = 120 exhibit a close match to the experimental data, particularly at the central markers (e.g., markers 4 and 5), where the displacement is highest.

In contrast, the results for α = 40 and α = 50 deviate significantly from the experimental data, with much higher displacements observed, indicating that these parameters do not accurately capture the mechanical behavior of the skin. The simulation for α = 90 and α = 100 shows moderate agreement but still exhibits slight deviations compared to the experimental reference. Overall, this figure highlights the importance of selecting appropriate Ogden parameters to ensure accurate modeling of skin deformation.

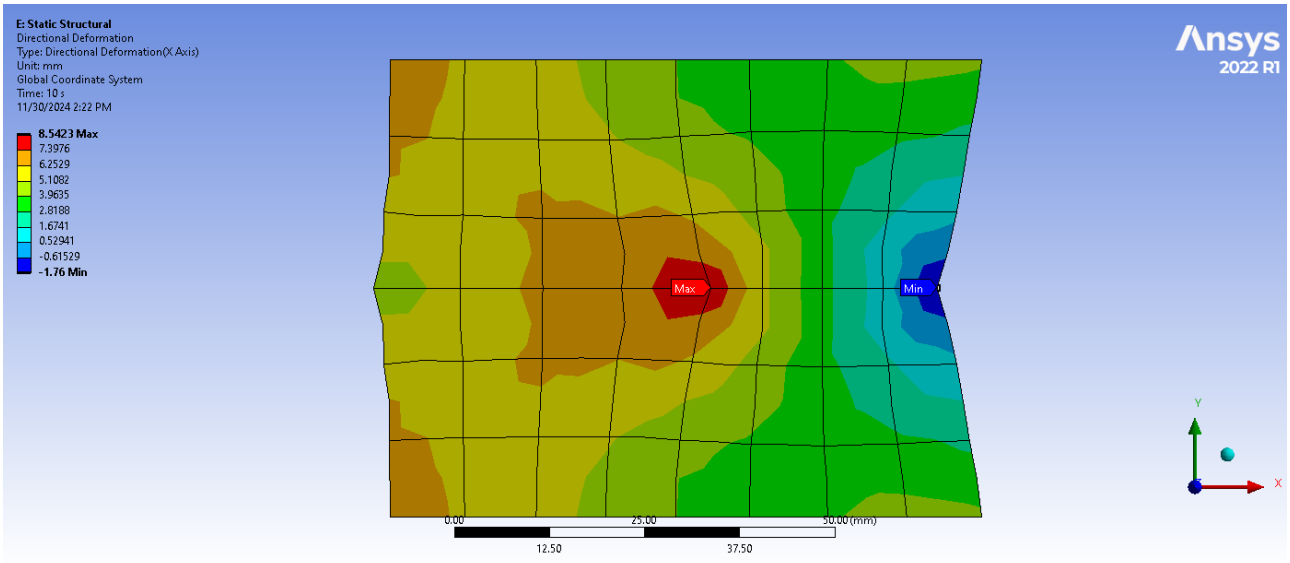

Figure 4.4 Total axial strain of the thin plate (Ogden material parameters μ = 10 Pa, α = 90)

Figure 4.4 presents the total axial strain distribution in a thin plate modeled with Ogden hyperelastic material parameters (μ = 10 Pa, α = 90). The color contour reveals a clear asymmetry in deformation across the plate, with the maximum tensile strain concentrated near the center-left region, shown in red, while the highest compressive strain appears on the mid-right side, shown in dark blue. The surrounding gradient transitions indicate how strain propagates from these extrema through the material. This strain pattern suggests a localized axial deformation response, likely due to uneven loading or boundary conditions.

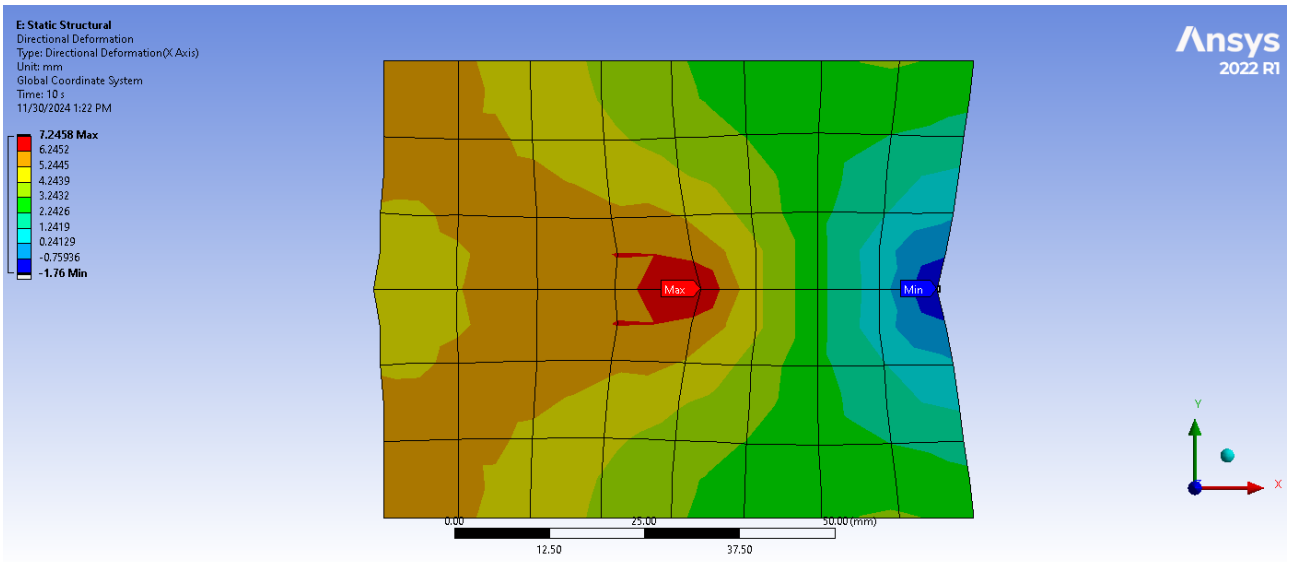

Figure 4.5 Total axial strain of the thin plate (Ogden material parameters μ = 10 Pa, α = 110)

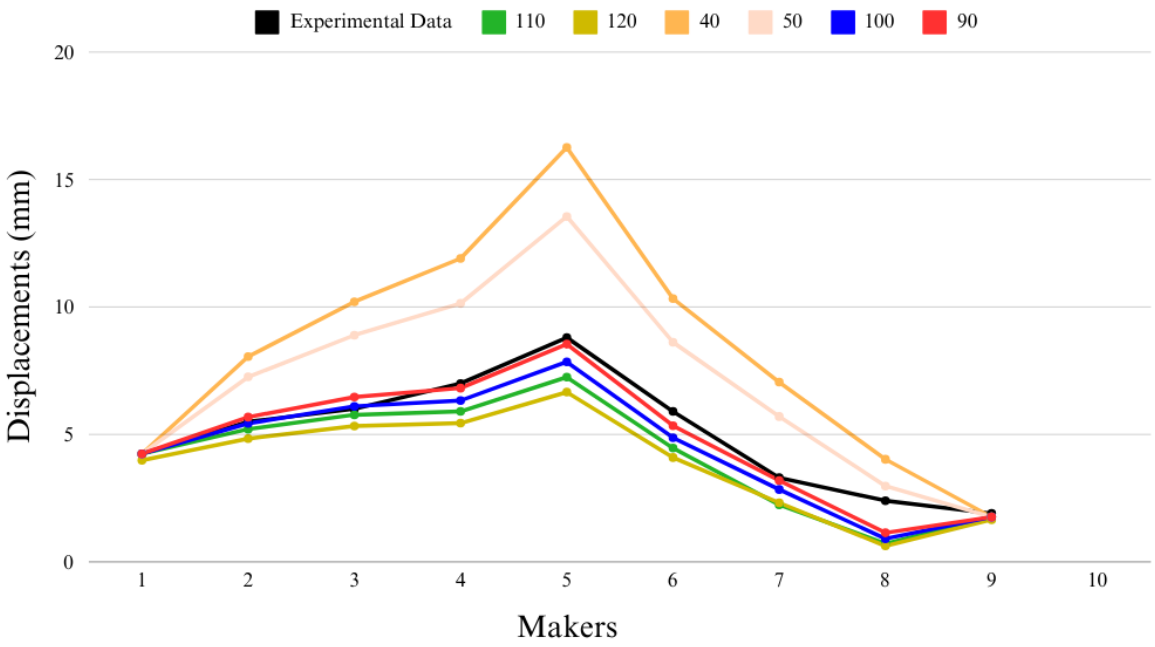

Figure 4.6 Comparison of simulation results (PLANE183 element, six sets of Ogden parameters, 48 elements) with reference data

4.5.1.2 2D model with medium-density element mesh

In the previous experiment, with a total of 48 elements (8 x 6 elements), the results indicated significant errors. In this analysis, the number of elements will be increased to 192 elements, using PLANE183 (16 x 12 elements). The load, boundary conditions, element type, and Ogden material parameters are identical to those specified in section 4.5.1.

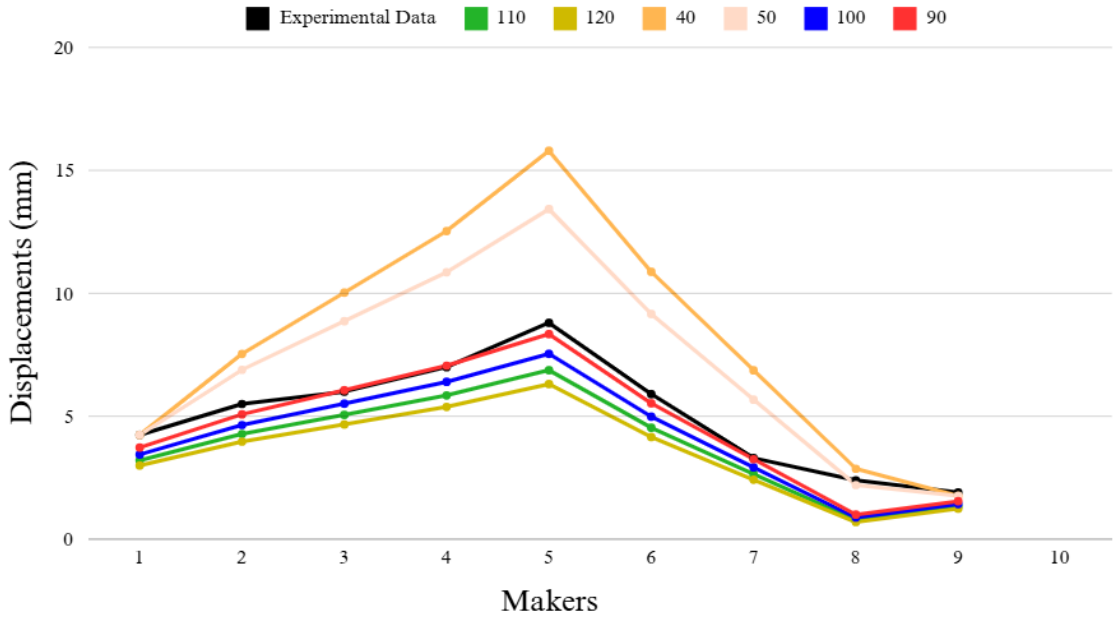

Figure 4.7 Comparison of simulation results (PLANE183 element, six sets of Ogden parameters, 192 elements) with reference data

4.5.2 Case 2: 3D human skin model

Most 2D models yield satisfactory results, but the current values are only relative, as a more generalized solution requires a 3D model of human skin. Therefore, based on the research parameters, the model has been expanded into a 3D problem (80 x 60 x 2 cm) to realize the applicability of the material under large deformations.

The simulation results show that the Ogden parameters mentioned above yield quite good results. Figure below shows the mechanical behavior of the skin divided into coarse mesh elements. The results indicate that the displacement has changed, making the skin more elastic. Although comparing the deformation results at second-order elements (experimental data and research data) showed higher displacement values than those at third-order elements (test data), the simulation image still demonstrates realistic behavior and clearly shows a bow wave effect.

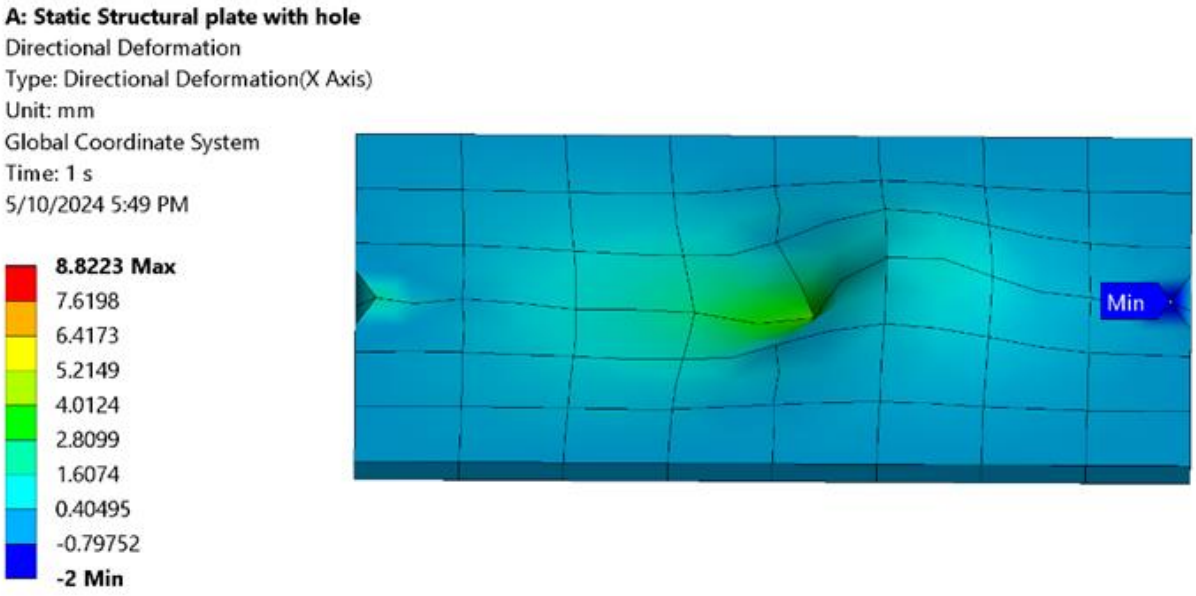

Figure 4.8 The behavior of skin directional deformation (x-axis), which has wrinkling

Figure 4.9 below illustrates the comparison between the simulation results of the research team and the results from previous studies. Experimental Data (Black Line) represents the reference displacement values collected from physical experiments. It serves as the benchmark for comparison with the simulated and test data. Test Data (Green Line) illustrates test results obtained from previous simulations or experiments under specific conditions. It shows significant deviations, particularly in the middle range of markers (e.g., from 4 to 6), where displacements peak and subsequently drop off. Present Data (Yellow

Line) shows the simulated results from the current study using the specified parameters (SOLID 186 and Ogden's model). The results closely align with the experimental data in both trend and magnitude, particularly at the peak displacement near marker 5 and the decreasing trend afterward.

In Jamaluddin Mahmud et. al.'s study, the results are empirical, whereas the simulation results from Thach Song Ngoc Dinh et. al. demonstrate the similarity of the second-order Ogden hyperelastic material. With the third-order Ogden material, the results indicate the structural rigidity of the material. This is a positive sign as the results show the presence of bow-wave phenomena in the third order, similar to the previous two results. Therefore, the use of this material can be applied to artificial human skin or utilized as a substitute material for other practical applications.

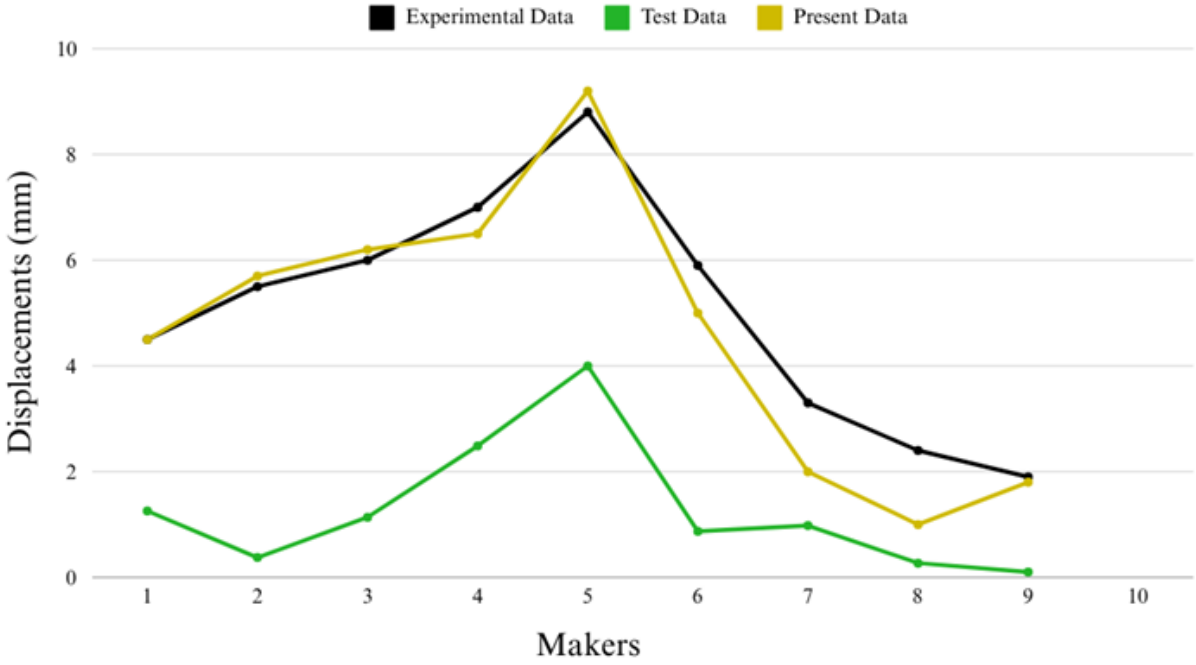

Figure 4.9 Compares the simulated results (SOLID 186, N = 3 of Ogden's parameters, 48 elements) to reference data

4.6 Evaluation of the results

The overall results indicate that third-order Ogden hyperelastic materials exhibit greater stiffness under load compared to their second-order counterparts. This suggests that artificial skin substitutes using third-order Ogden materials could effectively replicate the mechanical behavior of human skin, particularly in terms of tensile elasticity. Although the second-order model provides results that more closely align with reference data for real skin, extending the analysis to the third order enhances the model's robustness and increases

the likelihood of successful application in synthetic skin design. Therefore, exploring higher-order formulations not only broadens the design space but also improves confidence in the material's ability to withstand physiological mechanical demands.

In Chapter 4, the identification of material parameters plays a critical role, as it forms the foundational dataset for the subsequent simulation experiments presented in Chapter 5. These parameters are essential to validate the applicability of the Ogden hyperelastic material model within biomechanical contexts. By establishing a reliable material profile in this chapter, the study lays the groundwork for demonstrating, through simulation, that the Ogden model is a viable candidate for replicating the mechanical behavior of soft biological tissues in biomedical applications.

CHAPTER 5: THE MICROWAVE CAVITY ANALYSIS WITH MODEL

5.1 Variables of human skin to apply in simulation and boundary conditions

In this simulation, the model data and boundary conditions were covered in section 3.3. For Ansys HFSS, entering the input parameters correctly is crucial. The diagram 5.1 shows the step-by-step setup procedure in the simulation software.

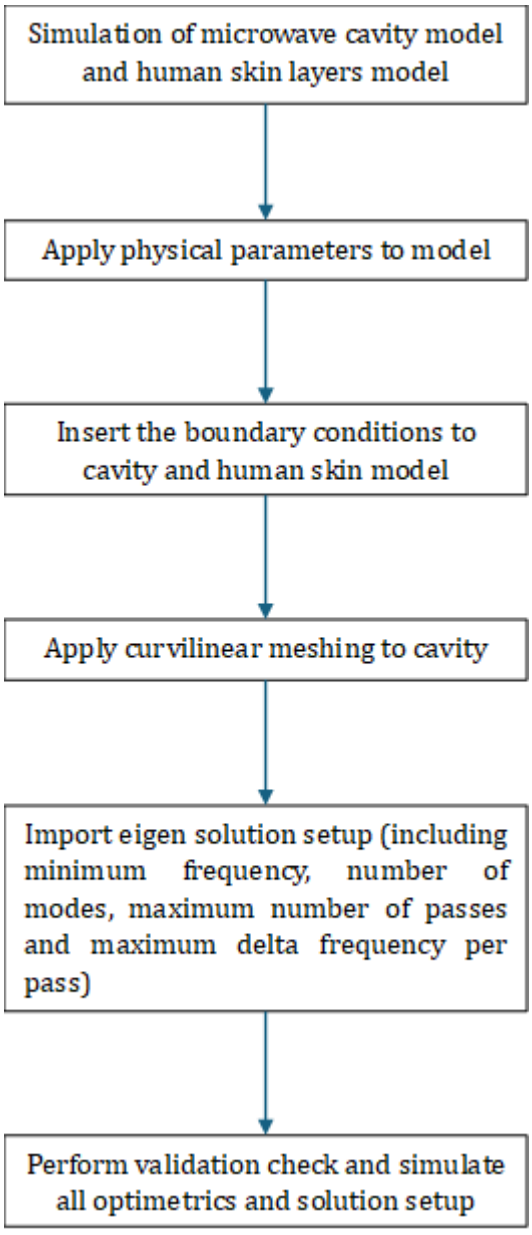

Fig 5.1 The main process in simulation the impact of microwave radiation on human skin

The main method uses in this model is Eigenmode solvers, which are employed to perform an analysis that does not rely on an external power source, characterizing it as an "undriven" approach. In this method, wave ports are not utilized, except when resistively loading a resonator for the purpose of determining the "loaded quality factor." The solver operates under the assumption that a certain quantity of energy is stored within the structure, and it subsequently identifies the resonant modes and their corresponding field distributions. Once the electromagnetic fields and surface currents are accurately characterized, the concept of finite conductivity is applied to the structure. This application enables the calculation of the resonator's quality factor (Q) through the established relationship between the stored energy and the energy dissipated per cycle.

5.2 Simulation results validating material parameters

The analysis results indicate that a convergence based on a pass number of 15 is sufficient, as HFSS criteria are based on the S-parameters at the ports. The S-parameter represents the integration of field intensity across the port surface. The number of solved elements fluctuates 15937 tetrahedral elements, depending on the established model. This ensures that the analysis results are detailed and clear, providing a high level of accuracy in the simulation, as a graph in figure 5.2.

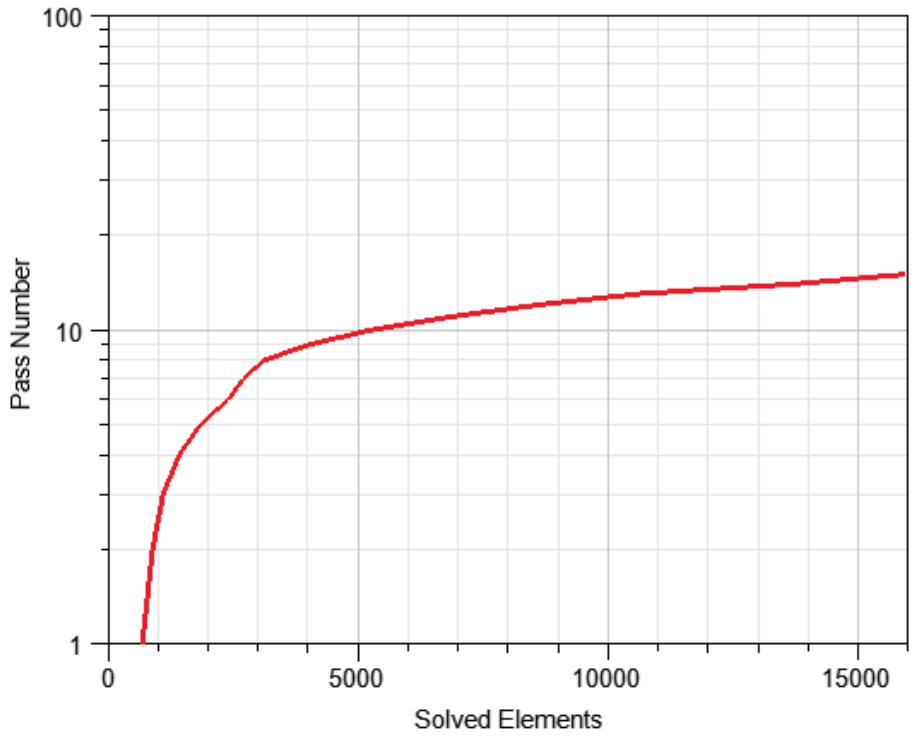

Figure 5.2 The convergence of pass number and solved elements at this experiment

The variability in tetrahedral size across regions suggests that the meshing is adapted to the complexity and importance of each area. The table 5.1 below shows that some valuables of mesh statistics calculate after meshing.

Table 5.1 The mesh statistics after validating and analyzing

Region	Num Tets	Min edge length	Max edge length	RMS edge length	Min tet vol	Max tet vol	Mean tet vol	Std Devn (vol)
Cavity	8083	1.75	20.40	6.08	0.08	188.09	11.75	16.71
Dermis	6072	1.19	4.05	2.38	0.12	2.91	0.66	0.36
Epidermis	1384	1.61	4.30	2.86	0.16	3.42	1.01	0.49
Hypodermis	398	2.28	5.00	3.50	0.07	0.89	0.30	0.13

5.2.1 Case 1: Low frequency (magnitude: 1020.800 V/m, frequency: 1.5 GHz, number of passes: 15)

The first layer to be analyzed is the epidermis of the human skin structure. At a frequency of 1.5 GHz, simulation results in figure 4 indicate that microwave energy has a significant impact on the skin. Because of the vector of radiation in cavity, four sides of model have the same impact of energy. As the energy penetrates through the skin layer, it gradually diminishes due to the presence of water within the body, which leads to the absorption of energy by water molecules. In a cavity, the presence of reflective surfaces can create standing waves, leading to non-uniform heating of the epidermis. Hot spots may develop where the electromagnetic field intensity is highest.

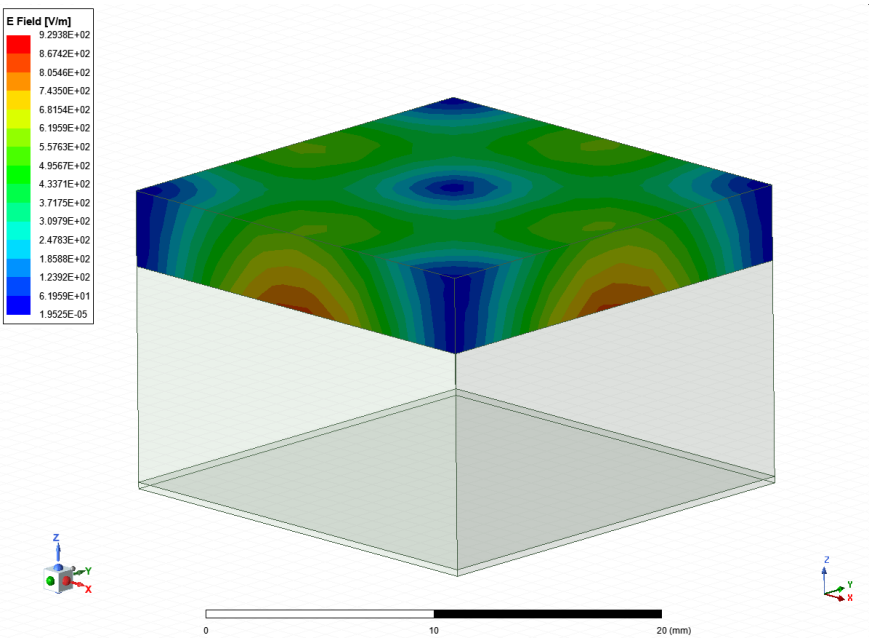

Figure 5.3 The epidermis layer at 1.5 GHz

The second layer to be analyzed is the dermis. After passing through the first layer, a portion of the energy has already been absorbed as figure 5.4, resulting in a reduction of electromagnetic energy in the second layer. Near the interface with the first layer, energy remains relatively not high at the central region, but it diminishes towards the periphery. On other surfaces of this layer, the energy distribution varies due to the differing conductivities between the two skin layers, leading to an uneven distribution of energy throughout the dermis.

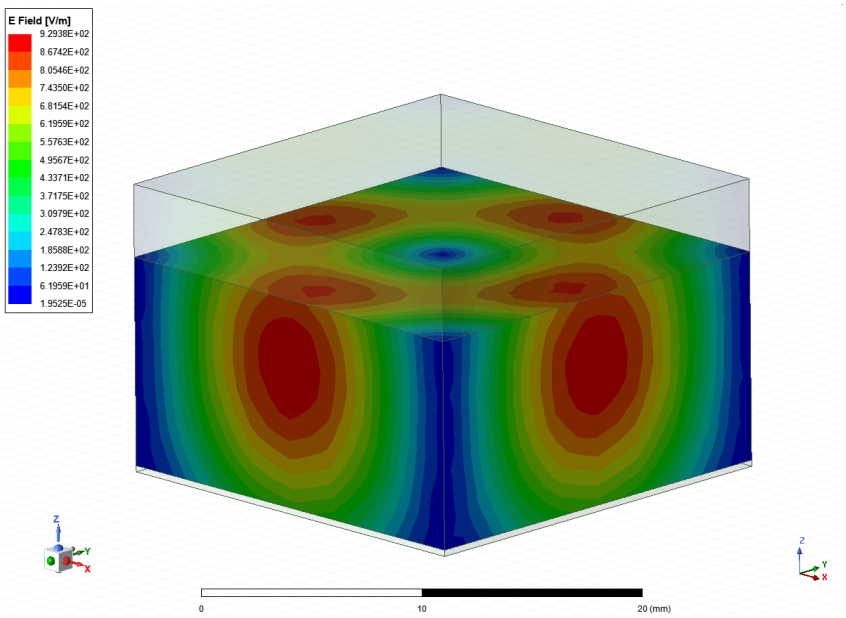

Figure 5.4 The dermis layer at 1.5 GHz

As the figure 5.5 is the final layer to be analyzed: the hypodermis, which is also the thinnest layer in the human skin structure and contains a significant amount of adipose tissue. Fat has a lower water content, leading to different permittivity and conductivity values compared to the other layers. Microwave energy passes from the dermis into the hypodermis. Since the cavity is enclosed, there is some additional energy reflected from the cavity frame reaching the bottom of this layer, but this contribution is minimal. The primary source of energy in this layer comes from the dermis, which disperses as it moves downward, resulting in a broader distribution of energy compared to the upper layers. However, the energy intensity at the surfaces of this layer is significantly reduced, as indicated by the lower values on the color scale.

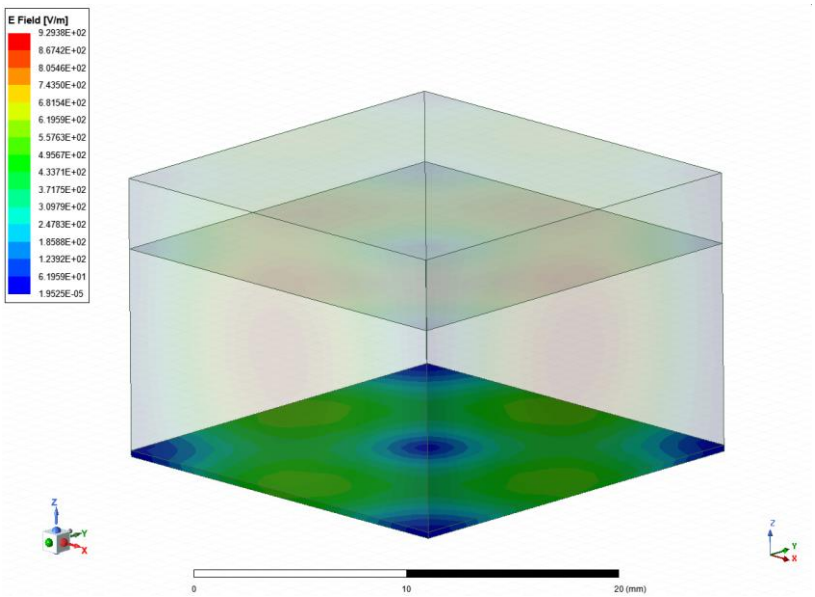

Figure 5.5 The hypodermis layer at 1.5 GHz

The approach to the microwave cavity seems to be less effective than expected. However, through simulations with applied material parameters, the results indicate a certain impact of microwave radiation on the human body. Additionally, the energy transfer from the top down through the skin layers or via the lateral surfaces of the model demonstrates varying levels of energy absorption across different layers of the skin, as illustrated in figure 5.6.

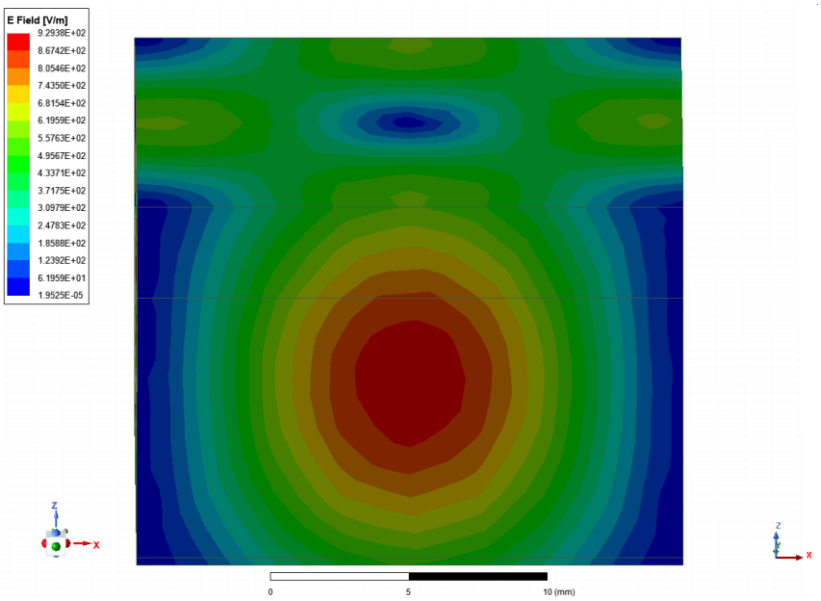

Figure 5.6 One side of three layers shows how the radiation gets through the model

5.2.2 Case 2: High frequency (magnitude: 1020.800 V/m, frequency: 3.0 GHz, number of passes: 15)

Higher microwave frequencies tend to penetrate materials more effectively rather than being absorbed. This leads to less efficient conversion of energy into heat compared to lower frequencies, resulting in reduced heating. Additionally, within the human body, water molecules are most effective at absorbing energy at a frequency of 2.45 GHz. However, when the energy level exceeds this optimal range, the efficiency of these molecules decreases, allowing the energy to pass through the material more easily. Consequently, the surface of the first skin layer, as demonstrate in figure 5.7, will absorb less microwave energy, resulting in greater energy penetration through the layers.

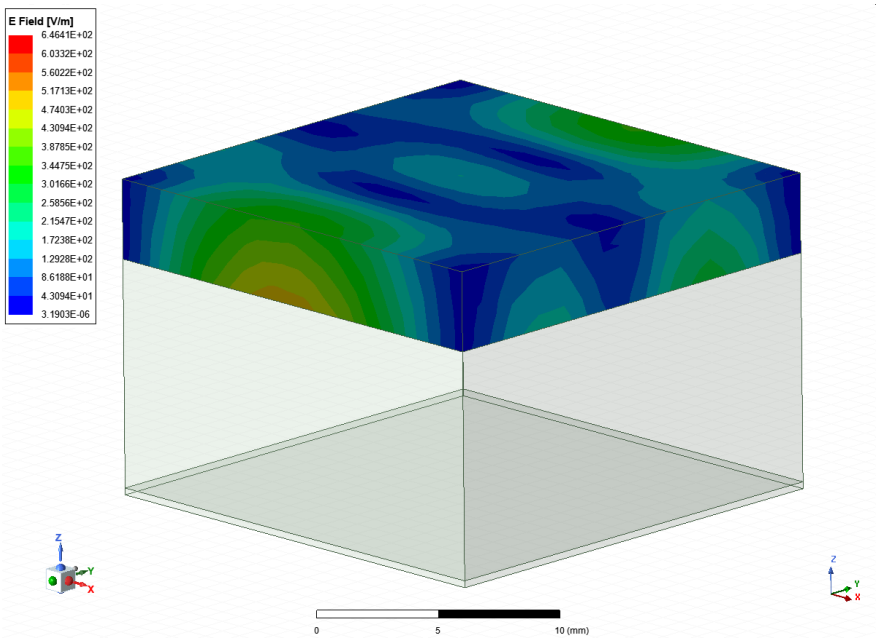

Figure 5.7 The epidermis layer at 3.0 GHz

Similarly, as energy passes through the second and third layers, a noticeable reduction in energy occurs as it penetrates the skin. As shown in figures 5.8 and 5.9, the energy received in these layers exhibits minimal changes compared to the energy observed in the first layer.

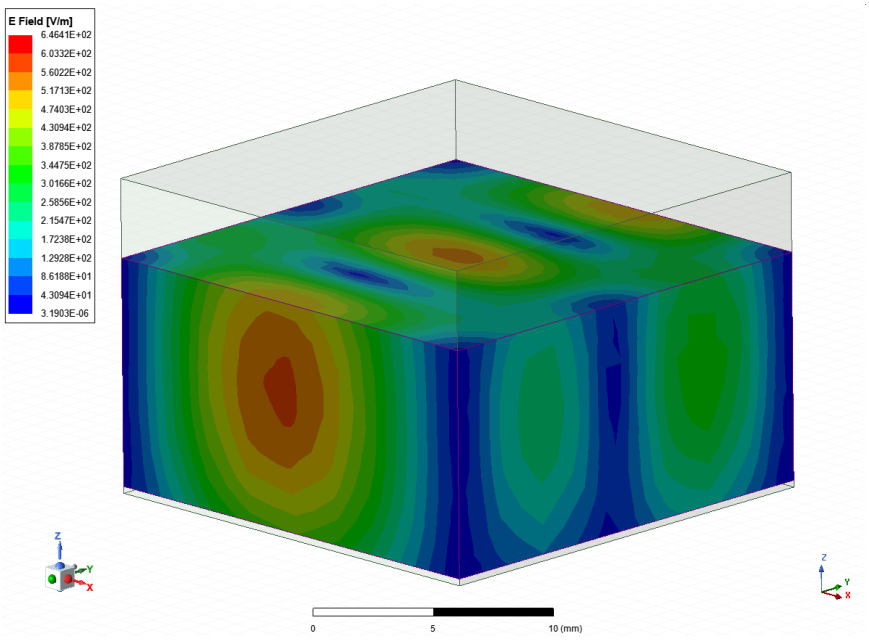

Figure 5.8 The dermis layer at 3.0 GHz

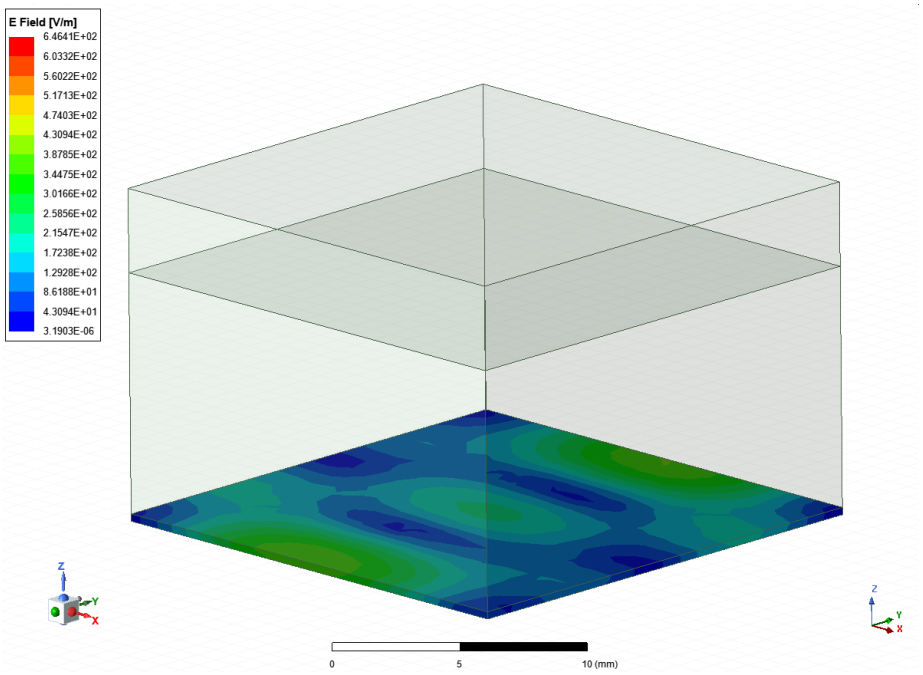

Figure 5.9 The hypodermis layer at 3.0 GHz

To validate the practical effects of the microwave cavity on the human body, the study on the impact of microwave radiation from mobile phone waves is cited to examine specific data [32]. Table 5.2 below presents a comparison and the equivalent percentage between the simulation study and the actual effects of microwave radiation under different approaches.

Table 5.2 The maximum value of E-field in simulation and comparison to references in 1mm

Layers/ Max E-field (V/m)	1.5 GHz			3 GHz		
	This study	Reference [32]	% error	This study	Reference [32]	% error
Epidermis	929.38	1020.368	8.92	560.22	1020.368	45.10
Dermis	929.38	1020.368	8.92	603.32	1020.368	40.87
Hypodermis	619.59	1020.368	39.28	403.94	1020.368	60.41

This result presents a comparison between the simulated maximum electric field (E-field) values and reference data [32] across three biological skin layers—epidermis, dermis, and hypodermis—at two frequencies: 1.5 GHz and 3 GHz. For the 1.5 GHz case, the simulation results show relatively low errors for the epidermis and dermis layers (both at 8.92%), suggesting that the model accurately captures E-field penetration in the upper layers of the skin. However, a significantly higher error (39.28%) is observed in the hypodermis,

indicating reduced model accuracy at greater depths. At 3 GHz, all errors increase markedly. The E-field values drop in the simulation, as expected due to increased absorption and reflection at higher frequencies, but the deviation from reference data becomes more pronounced—especially in the hypodermis, where the error reaches 60.41%. This trend implies that the simulation's capability to represent electromagnetic field behavior deteriorates with both increasing frequency and depth. One possible cause could be oversimplified assumptions in the dielectric property distribution or insufficient mesh resolution in deeper layers.

Table 5.3 The maximum value of E-field in simulation and comparison to references in 5mm

Layers/ Max E-field (V/m)	1.5 GHz			3 GHz		
	This study	Reference [32]	% error	This study	Reference [32]	% error
Epidermis	918.36	1018.644	9.84	864.25	1018.644	15.16
Dermis	902.76	1018.644	11.38	745.89	1018.644	26.77
Hypodermis	648.15	1018.644	36.37	651.23	1018.644	36.07

At 1.5 GHz, the error margins in Table 5.3 are slightly higher than those in Table 5.2 for the epidermis and dermis layers—rising from 8.92% to 9.84% for the epidermis and from 8.92% to 11.38% for the dermis. However, the hypodermis error decreases modestly from 39.28% in Table 5.2 to 36.37% in Table 5.3. This suggests that increasing the simulation depth improves the accuracy for deeper layers like the hypodermis, likely because a thicker model allows better field penetration representation and reduces truncation effects. At 3 GHz, which is more susceptible to attenuation, the simulation still shows improved performance in Table 5.3 over Table 5.2. The % error in the epidermis drops from 45.10% to 15.16%, and in the dermis from 40.87% to 26.77%. The hypodermis shows a slight improvement from 60.41% to 36.07%. This significant reduction in error across all layers indicates that simulating with a 5 mm thickness provides a more realistic electromagnetic field interaction at higher frequencies, where energy tends to be absorbed more superficially.

5.3 Evaluation of the results

Overall, the simulation images indicate that the microwave cavity provides a favorable environment for generating and sustaining microwave radiation. However, when compared to real-world conditions—such as the presence of air and airborne particulates—the results show minor discrepancies in the upper two skin layers and more significant deviations in the deepest layer. This can be attributed to the limited availability of detailed dielectric and structural parameters for human skin, which constrains the accuracy of simulation inputs. Moreover, the human skin is an inherently complex system composed not only of the epidermis and dermis but also of interconnected components such as cellular structures, blood vessels, and neural networks. These intricacies are not yet fully captured in the current modeling framework. Nevertheless, these challenges highlight a clear opportunity and motivation to further refine the model in future research. Expanding the simulation to include multi-layered, biologically realistic parameters could substantially improve the fidelity of artificial skin modeling in microwave exposure studies.

In Chapter 5, the simulation results demonstrate that employing the Ogden hyperelastic model yields promising outcomes for the use of artificial materials as potential substitutes for human skin. The numerical analysis of microwave radiation absorption confirms the feasibility of the proposed approach, even when using only basic input parameters such as geometry, density, and absorption characteristics. Although the current study models skin as a homogeneous, nonlinear material—an assumption that simplifies the inherently complex, multilayered nature of biological tissue—it provides a valuable foundation for future developments. One of the key challenges ahead lies in advancing this research toward more anatomically accurate simulations. This includes incorporating detailed layer-specific mechanical and dielectric properties to ensure that artificial skin analogues not only mimic the mechanical response but also replicate the functional behavior of real skin under electromagnetic exposure. Ultimately, the findings here serve as an important step toward developing structurally and functionally viable synthetic skin for biomedical and engineering applications.

CHAPTER 6: DISCUSSION AND CONCLUSION

6.1 Conclusion

This thesis results show an assessment of the ratio between second-order and third-order Ogden hyperelastic materials. Although there are discrepancies in the results, the mechanical properties remain valid for potentially replicating the structure of human skin. This is one of the anticipated findings of the research team. Based on the finite element model for human skin and the Ogden material parameters developed above, the following studies can conduct simulations for different regions on human skin and diversify the types of simulated computational tasks. However, experimental data is needed for different skin regions.

As microwave energy penetrates the skin layers, the uneven distribution of energy across the layers results in varying absorption rates, primarily concentrated in the central regions of each layer. The epidermis, due to its thinner structure and direct exposure to the external environment, absorbs the most energy, leading to a rapid increase in temperature. As the energy penetrates deeper into the dermis and hypodermis layers, the absorption rate decreases, though it remains sufficient to cause significant thermal effects. This can induce biological changes within the tissue, especially if the energy levels exceed safe thresholds. Therefore, understanding how microwave energy interacts with and impacts the structure of human skin is crucial, not only for assessing potential risks but also for developing effective protective measures against microwave exposure.

6.1.1 Advantages

For the first numerical experiment, rigorously identifying the material parameters is critical. Within the analytical framework chosen for the constitutive model, core descriptors—primarily the elastic modulus and the material's deformation response—will serve as benchmarks for comparison with measured data from real human skin. Where necessary, supplementary metrics such as Poisson's ratio, large-strain (hyper-elastic) behavior, and any relevant viscoelastic or poroelastic coefficients can be incorporated to further refine this comparison and improve the fidelity of the simulation.

For the second simulation campaign, the multilayer architecture of human skin is represented through several salient descriptors (layer thickness, dielectric dispersion, moisture content, etc.). In the present thesis we focus on modelling the microwave-

absorption behaviour of a selected hyper-elastic surrogate and benchmarking it against experimentally acquired in-vivo data. The numerical results show that, at short source–tissue separations, the surrogate's absorbed power density is almost indistinguishable from that recorded for real skin. As the wave traverses the stratified medium, however, each successive layer removes additional energy, so the residual power decays progressively rather than remaining quasi-uniform, as would be observed in a single-layer idealisation. These observations imply that the proposed material is a credible stand-in for human skin in near-field exposure studies, provided that the layer-by-layer attenuation is explicitly incorporated into the computational model and the material's dielectric profile is calibrated across the relevant frequency band.

6.1.2 Disadvantages

In the current model, human skin is idealised as a single, homogeneous hyper-elastic layer. Only the overall geometry and a limited set of bulk material constants have been substituted, and the simulation does not yet resolve the highly stratified, architecturally complex nature of real skin.

Moreover, the microwave-cavity analysis has so far been conducted under idealised, isothermal electromagnetic conditions. In practical scenarios, power deposition and field distributions are strongly modulated by temperature, ambient humidity, airflow, and other environmental factors. Accurately capturing these effects will require a multilayer viscporo-elastic skin representation coupled to a full thermodynamic model of the surrounding medium.

6.2 Discussion

To develop a more accurate finite element model of human skin, future studies need to consider additional characteristics of human skin (such as viscosity, anisot-ropy, etc.) to achieve appropriate simulation results. Furthermore, to obtain accurate experimental data, it is necessary to conduct "In vivo Skin Deformation Motion" experiments and use the data obtained to construct finite element models for human skin that closely resemble real-world models. The computational model and results of the paper can be applied to the field of biomechanics or contribute to the development of medical devices, as well as in other skin-related areas (such as car seat design, shaving razors, or the cosmetics industry).

Despite extensive research over the years, there remains a scarcity of data on the heating effects of RF energy on human tissues within the currently relevant frequency range. Existing studies have generally involved a small number of subjects, limited RF exposure parameters, and a narrow selection of body regions. These limitations are particularly concerning given that exposure limits are intended to protect against thermal hazards. This thesis has laid the groundwork for further research into the interaction between microwave cavities and the human body, particularly concerning the vulnerability of certain organs to high levels of microwave energy. These studies face significant challenges due to the lack of detailed data necessary for creating near-perfect simulations of the human body. Simulating scenarios involving high energy and large anatomical structures is particularly difficult due to the complexities involved in meshing and analyzing the vast number of elements required for accurate analysis.

APPENDIX: LIST OF SCIENTIFIC RESEARCH PUBLICATIONS

1. The international conference proceedings publication

1.1 Huy Tran Manh and **Khanh Dinh Hoang Duy**, "Harnessing the Self-Healing Effect of Terahertz Rays: Advancements and Applications," *2023 1st International Conference on Health Science and Technology (ICHST)*, *IEEE Xplore*, Ha Noi, Vietnam, 2023, pp. 1-6, Jun 2024, doi: 10.1109/ICHST59286.2023.10565312.

1.2 **Duy Khanh Dinh Hoang**, Trung Nghia Tran, Thien Tich Truong and Thanh Nha Nguyen, "Simulation of Mechanical Behavior for Human Skin Using Finite Element Method with the Third-Order Ogden Hyperelastic Model," *10th International Conference on the Development of Biomedical Engineering in Vietnam (BME10)*, *IFMBE Proceedings*, Binh Thuan, Vietnam, vol. 122, no. 1, Jun 2025.

2. The national conference proceedings publication

2.1 Khang Gia Trinh, Luan Thanh Vo, Du Anh Tran, **Duy Khanh Dinh Hoang** and Nha Thanh Nguyen, "Analysis of heat transfer in aluminium window frame," *Tuyển tập Công trình Khoa học Hội nghị Cơ học Toàn quốc Kỷ niệm 45 năm Thành lập Viện Cơ học (IMECH-45)*, Ha Noi, Vietnam, Aug, 2024.

3. Conference report

3.1 Vo Thanh Luan, Trinh Gia Khang, Tran Anh Du and **Dinh Hoang Duy Khanh**, "Finite Element Analysis of Heat Transfer in Multi-layered Structures," *The 14th OISP Science and Technology Symposium (OSTS14)*, Ho Chi Minh City, Vietnam, Jul 2024.

3.2 Khang Nguyen Phuc, Quynh Nguyen Gia, Thien Le Tran Thuan, Thuan Tran Ho Vinh, Thu Ngo Ngoc Anh, **Khanh Dinh Hoang Duy**, Tu Tran Anh and Khai Le Quoc, "Evaluation of Lable Noise, Feature Extraction and Classification of Electroencephalogram Signals based on Non-linear Analysis Techniques and Machine Learning Algorithms," *The International Symposium on Applied Science 2023 (ISAS-2023)*, Ho Chi Minh City, Vietnam, Oct 2023.

3.3 **Duy Khanh Dinh Hoang**, Trung Nghia Tran, Thien Tich Truong and Nha Thanh Nguyen, "Analysis and Simulation of Microwave Radiation on Human Skin

Layers Model using The Finite Element Method," *The International Symposium on Applied Science 2024 (ISAS-2024)*, Ho Chi Minh City, Vietnam, Oct 2024.

3.4 **Dinh Hoang Duy Khanh**, Nguyen Minh Khoi, Pham Viet Khiem, Tran Huynh Gia Huy and Le Quoc Khai, "Identification and Classification of Multi-label Brain Tumors using MATLAB Software integrated with Graphical User Interface based on Convolutional Neural Network and Deep Learning Algorithms," *The BME Innovation Competition 2024 (BMEIC24),* Ho Chi Minh City, Vietnam, Dec 2023.

REFERENCES

[1] M. Boer, E. Duchnik, R. Maleszka, and M. Marchlewicz, “Structural and Biophysical Characteristics of Human Skin in Maintaining Proper Epidermal Barrier Function,” *Advances in Dermatology and Allergology*, vol. 33, no. 1, pp. 1–5, 2016.

[2] F. Gruttmann and R. L. Taylor, “Theory and finite element formulation of rubberlike membrane shells using principal stretches,” *International Journal for Numerical Methods in Engineering*, vol. 35, no. 5, pp. 1111–1126, Sep. 1992.

[3] M. J. Lohr, G. P. Sugerman, S. Kakaletsis, E. Lejeune, and M. K. Rausch, “An introduction to the Ogden model in biomechanics: benefits, implementation tools and limitations,” *Philosophical Transactions of the Royal Society A: Mathematical, Physical and Engineering Sciences*, vol. 380, no. 2234, Aug. 2022.

[4] J. N. Tehrani, “Mooney-Rivlin Biomechanical Modeling of Lung with Inhomogeneous Material,” *Conference proceedings: ... Annual International Conference of the IEEE Engineering in Medicine and Biology Society. IEEE Engineering in Medicine and Biology Society. Conference*, vol. 2015, Aug. 2015.

[5] Z. Y. Guo, X. Q. Peng, and B. Moran, “Mechanical response of neo-Hookean fiber reinforced incompressible nonlinearly elastic solids,” *International Journal of Solids and Structures*, vol. 44, no. 6, pp. 1949–1969, Mar. 2007.

[6] E. J. Rayfield, “Finite Element Analysis and Understanding the Biomechanics and Evolution of Living and Fossil Organisms,” *Annual Review of Earth and Planetary Sciences*, vol. 35, no. 1, pp. 541–576, May 2007.

[7] H. R. Moghimi and Azadeh Alinaghi, “Microwaves as a Skin Permeation Enhancement Method,” *Springer eBooks*, pp. 161–174, Jan. 2017.

[8] S. N. Korobeynikov, A. Yu. Larichkin, and T. A. Rotanova, “Hyperelasticity models extending Hooke’s law from small to moderate strains and experimental verification of their scope of application,” *International Journal of Solids and Structures*, vol. 252, p. 111815, Oct. 2022.

[9] H. Altenbach, “Rheological Modeling—Historical Remarks and Actual Trends in Solid Mechanics,” *Advanced structured materials*, pp. 1–16, Jan. 2023.

[10] R. W. Ogden, “Large Deformation Isotropic Elasticity—On the Correlation of Theory and Experiment for Incompressible Rubberlike Solids,” *Rubber Chemistry and*

Technology, vol. 46, no. 2, pp. 398–416, May 1973.

[11] Y. Yao, S. Chen, and Z. Huang, "A generalized Ogden model for the compressibility of rubber-like solids," *Philosophical Transactions of the Royal Society A Mathematical Physical and Engineering Sciences*, vol. 380, no. 2234, Aug. 2022.

[12] F. M. Hendriks, D. Brokken, C. W. J. Oomens, D. L. Bader, and F. P. T. Baaijens, "The relative contributions of different skin layers to the mechanical behavior of human skin in vivo using suction experiments," *Medical Engineering & Physics*, vol. 28, no. 3, pp. 259–266, Apr. 2006.

[13] Z. Lotfollahi, "The anatomy, physiology and function of all skin layers and the impact of ageing on the skin," *Wound practice & research*, vol. 32, no. 1, Mar. 2024.

[14] O. G. Martinsen and Arto Heiskanen, *Bioimpedance and Bioelectricity Basics*. Elsevier, 2023.

[15] D. M. Pozar, *Microwave engineering*. Hoboken, Nj: Wiley, 2012.

[16] S. Takashima, *Electrical Properties of Biopolymers and Membranes,*. CRC Press, 1989.

[17] J. C. Lin, "Specific absorption rates (SARs) induced in head tissues by microwave radiation from cell phones," *IEEE Antennas and Propagation Magazine*, vol. 42, no. 5, pp. 138–139, Jan. 2000.

[18] ANSYS, "Engineering Simulation & 3D Design Software | ANSYS," *Ansys.com*, 2017. https://www.Ansys.com/

[19] Satish Kumar Chimakurthi, S. Reuss, M. Tooley, and S. Scampoli, "ANSYS Workbench System Coupling: a state-of-the-art computational framework for analyzing multiphysics problems," *Engineering with Computers*, vol. 34, no. 2, pp. 385–411, Nov. 2017.

[20] L. V. Tsap, D. B. Goldgof, and S. Sarkar, "Human skin and hand motion analysis from range image sequences using nonlinear FEM," *IEEE Nonrigid and Articulated Motion Workshop (in conjunction with IEEE Conference on Computer Vision and Pattern Recognition CVPR'97)*, pp. 80–88, Nov. 2002

[21] L. M. Tham, H. P. Lee, and C. Lu, "Cupping: From a biomechanical perspective," *Journal of Biomechanics*, vol. 39, no. 12, pp. 2183–2193, Jan. 2006.

[22] J. Mahmud, C. Holt, S. Evans, N. F. A. Manan, and M. Chizari, "A Parametric Study and Simulations in Quantifying Human Skin Hyperelastic Parameters," *Procedia*

Engineering, vol. 41, pp. 1580–1586, 2012.

[23] J. Mahmud, S. L. Evans, and C. A. Holt, “An Innovative Tool to Measure Human Skin Strain Distribution in Vivo using Motion Capture and Delaunay Mesh,” *Journal of mechanics*, vol. 28, no. 2, pp. 309–317, May 2012.

[24] J. Mahmud, "The Development of a Novel Technique in Measuring Human Skin Deformation in vivo to Determine its Mechanical Properties." *PhD Thesis, Cardiff University, UK*, 2009.

[25] J. Mahmud, C. A. Holt, and S. L. Evans, “An innovative application of a small-scale motion analysis technique to quantify human skin deformation in vivo,” *Journal of Biomechanics*, vol. 43, no. 5, pp. 1002–1006, Mar. 2010.

[26] D. S. N. Thach., N. T. Nha, L. S. Vay, T. T. Nghia and T. T. Thien, “Mechanical Behavior Simulation for Human Skin Using Finite Element Method”, *The 16th South East Asian Technical University Consortium (SEATUC)*, 2022.

[27] M. J. Peters, G. Stinstra, M. Hendriks, “Estimation of the Electrical Conductivity of Human Tissue,” *Electromagnetics*, vol. 21, no. 7–8, pp. 545–557, Sep. 2001.

[28] S. Gabriel, R. W. Lau, and C. Gabriel, “The dielectric properties of biological tissues: II. Measurements in the frequency range 10 Hz to 20 GHz,” *Physics in Medicine and Biology*, vol. 41, no. 11, pp. 2251–2269, Nov. 1996.

[29] M. Jones, “Microwave Cavity Simulation Using Ansys HFSS,” *Springer proceedings in physics*, pp. 1–7, Jan. 2020.

[30] P. Tong and Y. C. Fung, “The stress-strain relationship for the skin,” *Journal of Biomechanics*, vol. 9, no. 10, pp. 649–657, Jan. 1976.

[31] S. L. Evans, “On the implementation of a wrinkling, hyperelastic membrane model for skin and other materials,” *Computer Methods in Biomechanics & Biomedical Engineering*, vol. 12, no. 3, pp. 319–332, Feb. 2009.

[32] A. Verma, V. Kumar, and S. Gupta, “Bio-effects of 5th generation electromagnetic waves on organs of human beings,” *Global Health Journal*, vol. 7, no. 4, pp. 206–211, Dec. 2023.

VIETNAM NATIONAL UNIVERSITY HO CHI MINH CITY
HO CHI MINH CITY UNIVERSITY OF TECHNOLOGY
FACULTY OF APPLIED SCIENCE
DEPARTMENT OF
BIOMEDICAL ENGINEERING PHYSICS

SOCIALIST REPUBLIC OF VIETNAM
Independence – Freedom – Happiness

Ho Chi Minh City, May 05th, 2025

PROGRESS MONITORING TRACKING
CAPSTONE PROJECT

Student's full name: DINH HOANG DUY KHANH

Student's ID: 2153439

Address: 255/1, Group 3, Quarter 9, Tan Phong Ward, Bien Hoa City, Dong Nai Province, Vietnam

Email: khanh.dinhoisp2003@hcmut.edu.vn

Phone number: (+84) 981 863 824

Instructor 1 full name: Assoc. Prof. Dr. Tran Trung Nghia

Instructor 2 full name: Assoc. Prof. Dr. Nguyen Thanh Nha

Capstone project title: Investigation and Simulation of The Mechanical Behavior of Human Skin Layers with The Hyperelastic Model using The Finite Element Method

Week	**Date**	**Workload**		**Instructors's approval**
		Completed	**Continuing**	
1	06/01/2025	Discuss with instructors	Literature review	
2	13/01/2025	Read the references	Discuss with instructors	
3	03/02/2025	Build the microwave cavity	Check the cavity parameters	
4	10/02/2025	Build the human skin model	Check the model parameters	
5	17/02/2025	Connect 2 models	Check the method	
6	24/02/2025	Write the report	Simulation and result	
7	03/03/2025	Simulation and result	Check the variables	
8	17/03/2025	Simulation and result	Check the variables	
9	24/03/2025	Compare to references	Check the figures	
10	31/03/2025	Write the report	Write report	
11	07/04/2025	Write the report	Prepare for presentation	
12	14/04/2025	Midterm checkpoint presentation		
13	21/04/2025	Fixing the report	Give to instructors	
14	28/04/2025	Final revision and formatting	Give to instructors	
15	05/05/2025	Submit to instructors and faculty		